

REPORT DOCUMENTATION PAGE					Form Approved OMB No. 0704-0188	
<p>The public reporting burden for this collection of information is estimated to average 1 hour per response, including the time for reviewing instructions, searching existing data sources, gathering and maintaining the data needed, and completing and reviewing the collection of information. Send comments regarding this burden estimate or any other aspect of this collection of information, including suggestions for reducing the burden, to Department of Defense, Washington Headquarters Services, Directorate for Information Operations and Reports (0704-0188), 1215 Jefferson Davis Highway, Suite 1204, Arlington, VA 22202-4302. Respondents should be aware that notwithstanding any other provision of law, no person shall be subject to any penalty for failing to comply with a collection of information if it does not display a currently valid OMB control number.</p> <p>PLEASE DO NOT RETURN YOUR FORM TO THE ABOVE ADDRESS.</p>						
1. REPORT DATE (DD-MM-YYYY)		2. REPORT TYPE		3. DATES COVERED (From - To)		
12-03-2007		Final		02-15-2005 to 08-31-2007		
4. TITLE AND SUBTITLE Computational Simulation of High Speed Projectiles in Air, Water, and Sand					5a. CONTRACT NUMBER N00014-05-1-0224	
					5b. GRANT NUMBER	
					5c. PROGRAM ELEMENT NUMBER	
6. AUTHOR(S) Jack R. Edwards (NCSU)					5d. PROJECT NUMBER	
					5e. TASK NUMBER	
					5f. WORK UNIT NUMBER	
7. PERFORMING ORGANIZATION NAME(S) AND ADDRESS(ES) North Carolina State University, 8 Holliday Hall, Campus Box 7214, Raleigh, NC 27525					8. PERFORMING ORGANIZATION REPORT NUMBER	
9. SPONSORING/MONITORING AGENCY NAME(S) AND ADDRESS(ES) Office of Naval Research 875 North Randolph Street Arlington, VA 22203-1995					10. SPONSOR/MONITOR'S ACRONYM(S)	
					11. SPONSOR/MONITOR'S REPORT NUMBER(S)	
12. DISTRIBUTION/AVAILABILITY STATEMENT Approved for Public Release; distribution is Unlimited						
13. SUPPLEMENTARY NOTES						
14. ABSTRACT <p>The development of a comprehensive computational fluid dynamics approach for conducting simulations of projectile penetration into water-saturated sand is reported. High resolution upwind schemes suitable for a fluid dynamic system consisting of gas, liquid, and dispersed solids phases are derived and are combined with a time-derivative preconditioning strategy for efficient time integration at all flow speeds. A solids-stress model based on Mohr-Coulomb critical-state theory is used to account for compaction and deformation of sand during projectile penetration. An overset-mesh framework is also implemented in order to handle projectile relative motion in subsequent work, and improved phase interface capturing methods are also developed and tested. Results are presented for two sets of experimental data involving projectile penetration into dry sand. The computational results are sensitive to the solids-stress model and the drag coefficient predictions are generally lower than indicated in the experimental data.</p>						
15. SUBJECT TERMS Surf-zone clearance, two-phase flow models, granular stress tensor,						
16. SECURITY CLASSIFICATION OF:			17. LIMITATION OF ABSTRACT UL	18. NUMBER OF PAGES	19a. NAME OF RESPONSIBLE PERSON	
a. REPORT unclassified	b. ABSTRACT unclassified	c. THIS PAGE unclassified			Jack R. Edwards	
					19b. TELEPHONE NUMBER (Include area code) 919-515-5264	

Computational Simulation of High-Speed Projectiles in Air, Water, and Sand

Final Technical Report

Office of Naval Research
Grant Number: N000140510224

Submitted by

Jack R. Edwards
Department of Mechanical and Aerospace Engineering
North Carolina State University
Raleigh, NC 27695
Phone: (919) 515-5264 Fax (919) 515-7968 E-mail: jredward@eos.ncsu.edu

To

Office of Naval Research
(Attn. Mr. Brian Almquist)
875 North Randolph Street
Arlington, VA 22203-1995

20071217489

TABLE OF CONTENTS

<u>Section</u>	<u>Page Numbers</u>
Table of Contents	2
Abstract	3
1. Background and Objectives	4
2. Governing Equations	5-10
2.1. Fluid Closure Relations	5-6
2.2. Sand Closure Relations	6-9
2.3. Interchange Terms	9-10
3. Numerical Methods	10-16
3.1. Eigenvalue Analysis	10-11
3.2. Low Diffusion Upwinding Methods	11-13
3.3. Time Integration Scheme	13-14
3.4. Arbitrary Lagrangian /Eulerian Formulation	14
3.5. Overset Mesh Framework	14-15
3.6. Sharp Interface Capturing	15-16
3.7. Grid Arrangement	16
4. Results	16-21
4.1. Water Entry	16-17
4.2. Sand Entry – Configuration II	17-18
4.3. Sand Entry – Configuration III (Initial Results)	18-19
4.4. Sand Entry – Configuration III (Later Results)	19
4.5. Sand Entry – Configuration III-D	20
4.6. Overset Mesh Results – Configuration III-D	20-21
5. Conclusions	21
Publications	21
Personnel	21-22
References	22-23
Figures	24-33

Abstract

The development of a comprehensive computational fluid dynamics approach for conducting simulations of projectile penetration into water and dry sand is reported. High resolution upwind schemes suitable for a fluid dynamic system consisting of gas, liquid, and dispersed solids phases are derived and are combined with a time-derivative preconditioning strategy for efficient time integration at all flow speeds. A solids-stress model based on Mohr-Coulomb critical-state theory is used to account for compaction and deformation of sand during projectile penetration. An overset-mesh framework is also implemented in order to handle projectile relative motion in subsequent work, and improved phase interface capturing methods are also developed and tested. Results are presented for two sets of experimental data involving projectile penetration into dry sand. The computational results are sensitive to the solids-stress model and the drag coefficient predictions are generally lower than indicated in the experimental data.

1. Background and Objectives

A problem of great interest for naval applications is the water and/or sand entry problem for high-speed projectiles. Supercavitating projectiles can be used for underwater mine neutralization, beach and surf zone mine clearance, littoral ASW, and neutralizing combat swimmers. Many current and possible future systems must deal with a high-speed water entry: RAMICS, VENOM, HYDRA, SEA SNIPER, JABS, and anti-combat swimmer systems. The water entry phase of flight is interesting and challenging due to projectile transitioning from flight in air to supercavitated flight through water. For the beach/surf zone clearance application, projectiles/bombs are designed to enter the water and sand vertically, so that an axisymmetric approximation to the flowfield may be appropriate if the projectile is stable. Investigating projectile stability will require a fully three-dimensional approach with a six-degree of freedom (6-DOF) algorithm. Projectile stability should be a strong function of supercavity size, shape, and unsteadiness. The supercavity is largely determined by velocity and nose shape. The nose shape of a penetrator is generally a compromise between lethality and cavity generation concerns, with minimizing drag in air being a tertiary consideration.

The overall goal of the presented work is to develop the ability to predict velocity and penetration depths in water and/or sand of a penetrator or bomb after a vertical water entry. The work seeks to develop new algorithms for simulating the water and sand entry phases of high-speed projectiles. The ability to accurately predict velocity and penetration depth is critical to lethality of systems that require a maximum/minimum velocity on impact or a specific sand penetration depth. The current work develops high-resolution upwinding schemes and time-derivative preconditioning techniques suitable for a fluid-dynamic system consisting of gas (air or cavitated water), liquid (water), and dispersed solid (sand) phases. Such techniques will facilitate sharp capturing of phase interfaces and vortical structures at all flow speeds and under all states of compressibility, thus enabling high-fidelity predictions of the forces and moments acting upon high-speed projectiles under transient conditions.

The technical approach combines the air / water two-phase flow Navier-Stokes codes developed by NSWC-PC and NCSU [1-6] with the dense gas / solid fluidization codes developed at NCSU [7,8] to yield a unified procedure capable of capturing the detailed physics of projectile penetration into water and into dry sand. The complete algorithm allows detailed modeling of granular flow effects, such as solids stresses, and captures phase interfaces as part of the solution. Velocity slip effects, solids compaction, and cavity bubble formation and collapse are accounted for in the model. The new algorithm utilizes time-derivative preconditioning as a way of reconciling the widely-varying characteristic speeds found in this three-phase system, thus enabling efficient integration at all flow speeds and all states of compressibility. To enable eventual application of the code in six-degree of freedom simulations, the procedure is embedded within an overset-mesh framework using the SUGGAR/DiRTLlib [9,10] protocol. The sections that follow describe the governing equations, the numerical methods used to solve them, and the results of this investigation, followed by some concluding remarks.

2. Governing Equations

The governing equations for the three-phase system (fluid (air + water) and sand) may be written in tensor notation as follows

Fluid phase:

$$\text{vapor mass: } \theta_f Y_v \frac{\partial p}{\partial \tau} + \frac{\partial(\rho_f \alpha_f Y_v)}{\partial t} + \frac{\partial(\rho_f \alpha_f Y_v u_{j,f})}{\partial x_j} = 0 \quad (1)$$

$$\text{fluid mass: } \theta_f \frac{\partial p}{\partial \tau} + \frac{\partial(\rho_f \alpha_f)}{\partial t} + \frac{\partial(\rho_f \alpha_f u_{j,f})}{\partial x_j} = 0 \quad (2)$$

$$\text{fluid momentum: } \theta_f u_{i,f} \frac{\partial p}{\partial \tau} + \frac{\partial(\rho_f \alpha_f u_{i,f})}{\partial t} + \frac{\partial(\rho_f \alpha_f u_{i,f} u_{j,f} - \tau_{ij,f})}{\partial x_j} = -\alpha_f \frac{\partial p}{\partial x_i} + \rho_f \alpha_f g_i + S_{\text{mom},i} \quad (3)$$

$$\text{fluid energy: } \theta_f H_f \frac{\partial p}{\partial \tau} + \frac{\partial(\rho_f \alpha_f H_f)}{\partial t} - \alpha_f \frac{\partial p}{\partial t} + \frac{\partial(\rho_f \alpha_f H_f - \tau_{jk,f} u_{k,f} - q_f)}{\partial x_j} = \rho_f \alpha_f u_{i,f} g_i - S_{\text{energy}} \quad (4)$$

Solids phase:

$$\text{solids mass: } \theta_s \frac{\partial p_s}{\partial \tau} + \frac{\partial(\rho_s \alpha_s)}{\partial t} + \frac{\partial(\rho_s \alpha_s u_{j,s})}{\partial x_j} = 0 \quad (5)$$

$$\text{solids momentum: } \rho_s \alpha_s \left(\frac{\partial u_{i,s}}{\partial t} + u_{j,s} \frac{\partial u_{i,s}}{\partial x_j} \right) = -\alpha_s \frac{\partial p}{\partial x_i} + \frac{\partial T_{ij}}{\partial x_j} + \rho_s \alpha_s g_i - S_{\text{mom},i} \quad (6)$$

$$\text{solids energy: } \rho_s \alpha_s C_{p,s} \left(\frac{\partial T_s}{\partial t} + u_{j,s} \frac{\partial u_{i,s}}{\partial x_j} \right) = S_{\text{energy}} \quad (7)$$

The subscripts v , f , and s represent vapor, fluid, and solids, respectively. The density is denoted by ρ , the velocity in coordinate direction i by u_i , the volume fraction by α , the vapor mass fraction (relative to the mass of the fluid phase) by Y_v , the pressure by p , the fluid and solid temperatures by T and T_s , and the gravitational acceleration vector by g_i . The terms involving $\frac{\partial}{\partial \tau}$ are associated with the time-derivative preconditioning method discussed in Section 3. The system is solved for $V = [Y_v, p, u_{i,f}, T, \alpha_s, u_{i,s}, T_s]$. Other variables are defined in the next section.

2.1. Fluid Closure Relations

Closure of the above system is achieved by applying suitable equations of state for the three phases. For the fluid phase, the following thermodynamic relations hold:

$$\text{Amagat's law: } \frac{1}{\rho_f} = \frac{Y_v}{\rho_v(p, T)} + \frac{1 - Y_v}{\rho_l(p, T)} \quad (8)$$

$$\text{Mixture total enthalpy: } H_f = Y_v h_v(T) + Y_l h_l(p, T) + \frac{1}{2}(u^2 + v^2 + w^2) \quad (9)$$

$$\text{Vapor phase equations of state: } \rho_v = p/(R_v T), \quad h_v = h_v(T) \quad [11] \quad (10)$$

Liquid water equations of state (modified Tait equation):

$$\begin{aligned} \rho_l &= \rho_{l,sat}(T)[1 + \frac{1}{3 \times 10^8}(p - p_{sat}(T))]^{1/7}, \\ h_l &= h_l(T) + \frac{(p - 101325)}{\rho_l} \end{aligned} \quad (11)$$

Saturation-state values (subscript ‘sat’) are obtained from [12] and the liquid reference enthalpy is obtained from [11].

The fluid stress tensor is modeled as

$$\begin{aligned} \tau_{ij,f} &= 2\mu_f \alpha_f S_{ij,f}, \\ S_{ij,s} &= \frac{1}{2} \left(\frac{\partial u_{i,f}}{\partial x_{j,f}} + \frac{\partial u_{j,f}}{\partial x_{i,f}} \right) - \frac{1}{2} \frac{\partial u_{k,f}}{\partial x_{k,f}} \delta_{ij} \end{aligned} \quad (12)$$

with the fluid viscosity formulated as

$$\mu_f = \alpha_v \mu_v(T) + \alpha_l \mu_l(T). \quad (13)$$

Here, α_v is the volume fraction of the vapor, relative to the fluid volume. The vapor and liquid viscosities are obtained from [11] and [13], respectively.

2.2. Sand Closure Relations

For the sand (granular) phase, the intrinsic sand density ρ_s is taken to be 2676.605 kg/m³. The solids stress tensor T_{ij} is defined as

$$T_{ij} = -p_s \delta_{ij} + \mu_s S_{ij,s}, \quad (14)$$

where the solids viscosity μ_s is expressed as a combination of a Newtonian viscosity and a non-Newtonian Mohr-Coulomb [14-17] viscosity that requires that the frictional stresses exhibit a zero-order dependence on the fluid strain rate. Considering the solids pressure as the critical-state pressure leads to the requirement that

$$\mu_s = \mu_{s,N} + \frac{p_s \sin(\phi)}{\sqrt{S : S|_s + \varepsilon/d_p^2}}, \quad (15)$$

where ϕ is the angle of internal friction (taken as zero or 28 degrees, depending on whether solids shear stresses are included. The strain-rate tensor for the solids phase is given as

$$S_{ij,s} = \frac{1}{2} \left(\frac{\partial u_{i,s}}{\partial x_{j,s}} + \frac{\partial u_{j,s}}{\partial x_{i,s}} \right) - \frac{1}{2} \frac{\partial u_{k,s}}{\partial x_{k,s}} \delta_{ij} \quad (16)$$

and the second invariant of the strain-rate tensor is

$$S : S|_s = S_{12,s} S_{12,s} + S_{13,s} S_{13,s} + S_{23,s} S_{23,s} - S_{11,s} S_{22,s} - S_{11,s} S_{33,s} - S_{22,s} S_{33,s} \quad (17)$$

The term ε/d_p^2 ($\varepsilon = 1 \times 10^{-4}$, $d_p = 0.00240$ m) is used to prevent divide-by-zero in uniform regions of the flow. The solids-stress model can be viewed as the distribution of the solids pressure in different directions depending on the elements of $S_{ij,s}$. Thus, it is appropriate to enforce the constraint that

$$-1 \leq \frac{S_{ij,s}}{\sqrt{S : S|_s} + \varepsilon/d_p^2} \leq 1 \quad (18)$$

for the non-Newtonian part of the stress tensor. As Mohr-Coulomb – type granular-flow models are known to be intrinsically unstable at short wavelengths [18], it is necessary to include a Newtonian viscosity to regularize the solution and to prevent unphysical behavior. We have adopted a simple model based on a von Neumann stability analysis:

$$\mu_{s,N} = C_{s,N} \sin(\phi) \rho_s \alpha_s a_s \Delta, \quad (19)$$

where Δ is a characteristic mesh-cell dimension in a particular coordinate direction, $C_{s,N}$ is a model constant, and a_s is a sound speed associated with the granular phase. This sound speed is defined as

$$a_s^2 = \frac{1}{\rho_s} \frac{\partial p_s}{\partial \alpha_s} \quad (20)$$

Results presented later illustrate the effect of varying the model constant $C_{s,N}$ on the predictions.

The solids pressure p_s must be defined in order to complete the formulation of the solids stress tensor. The solids pressure is near zero when the particles are in a dilute state but increases rapidly to giga-Pascal levels as the sand particles are compacted, then fragmented, by the applied load. We have used two techniques to model the response of dry sand considered in Lockheed-Martin's experiments in this study. In the first, we use an approach based on the Cooper-Eaton equation for powder compaction. [19] The Cooper-Eaton equation relates the solids pressure (identified as the trace of the solids stress tensor) to the volume fraction and has the general form

$$\tilde{\alpha}_s = \frac{\alpha_s - \alpha_{s,0}}{\alpha_{s,max} - \alpha_{s,0}} = A_1 \exp(-B_1 / p_s) + A_2 \exp(-B_2 / p_s), \quad (21)$$

where α_s is the solids volume fraction and p_s is the solids pressure. The Cooper-Eaton equation is valid for solids volume fraction values greater than an initial unloaded value $\alpha_{s,0}$. As written above, the Cooper-Eaton equation is implicit in the solids pressure. To avoid having to solve a non-linear equation, we have re-written the model as

$$\tilde{\alpha}_s = \frac{\alpha_s - \alpha_{s,0}}{\alpha_{s,max} - \alpha_{s,0}} = A_1 \exp(-B_1 / p_s) \left[1 + \frac{A_2 \exp(-B_2 / p_s)}{A_1 \exp(-B_1 / p_s)} \right] \quad (22)$$

and have curve-fitted the term in brackets as a fourth-order polynomial:

$$\begin{aligned} g(\tilde{\alpha}_s) &= \left[1 + \frac{A_2 \exp(-B_2 / p_s)}{A_1 \exp(-B_1 / p_s)} \right] = 1, \quad \tilde{\alpha}_s < 0.4 \\ g(\tilde{\alpha}_s) &= \left[1 + \frac{A_2 \exp(-B_2 / p_s)}{A_1 \exp(-B_1 / p_s)} \right] = a_1 + a_2 \tilde{\alpha}_s + a_3 \tilde{\alpha}_s^2 + a_4 \tilde{\alpha}_s^3 + a_5 \tilde{\alpha}_s^4, \quad \tilde{\alpha}_s > 0.4 \end{aligned} \quad (23)$$

This enables an explicit solution for the solids pressure:

$$p_{s,C-e,1} = \frac{B_1}{\ln\left(\frac{\tilde{\alpha}_s}{g(\tilde{\alpha}_s)}\right) - \ln(A_1)} \quad (24)$$

To extend the Cooper-Eaton equation smoothly beyond the assumed loading condition $\alpha_s = \alpha_{s,0}$, the following combined form is used:

$$p_{s,C-e,2} = \exp(\ln(p_{s,C-e,1} |_{\tilde{\alpha}_s=0.15}) - \frac{d \ln(p_{s,C-e,1} |_{\tilde{\alpha}_s=0.15})}{d \tilde{\alpha}_s} (\tilde{\alpha}_s - 0.15), \tilde{\alpha}_s < 0.15) \quad (25)$$

$$p_{s,C-e,2} = p_{s,C-e,1}, \tilde{\alpha}_s \geq 0.15$$

For volume-fraction values less than $\alpha_{s,0}$, we use the Boivin, et al. solids pressure model:

$$p_{s,B} = \rho_s C_{s,B} [\alpha_s + 2\alpha_{s,max,B} \ln(1 - \frac{\alpha_s}{\alpha_{s,max,B}}) - \frac{\alpha_s \alpha_{s,max}}{\alpha_s - \alpha_{s,max,B}}] \quad (26)$$

and then blend between the two to yield the final form for the solids pressure:

$$p_s = \exp\{\ln(p_{s,B}) + \frac{1}{2}[1 + \tanh(100(\alpha_s - \alpha_{s,0}))](\ln(p_{s,C-e,2}) - \ln(p_{s,B}))\} \quad (27)$$

Values for the constants in the Cooper-Eaton model were initially taken from data given for silicon dioxide in [19] (Model I) and were then least-squares re-fitted to match sand compaction data obtained by Lockheed-Martin [20] (Model II). These values are shown in Table 1, and the resulting composite solids-pressure profiles are shown in Figure 1.

Table 1: Parameters for Cooper-Eaton Solids-Pressure Models

Parameter	Model I value	Model II value
$\alpha_{s,0}$	varies depending on the case	varies depending on the case
$\alpha_{s,max}$	0.93	0.93
A_1	0.6	0.6528
B_1	17.232 (MPa)	67.033 (MPa)
a_1	-4.1175	-4.1175
a_2	32.8372	32.8372
a_3	-96.1131	-96.1131
a_4	121.4415	121.4415
a_5	-55.1670	-55.1670
$C_{s,B}$	1.397	1.397
$\alpha_{s,max,B}$	1.0	1.0

In some of the later calculations, we have used another fitting of the Lockheed-Martin sand compaction data in an attempt to provide a sharper transition between loaded / unloaded states and thereby improve drag predictions. This approach is defined by the following:

$$p_s = C_{M2} \{ A_{M1} [(\frac{\alpha_s}{\alpha_{sI}})^{B_{M1}} - 1] + A_{M2} [(\frac{\alpha_s}{\alpha_{sI}})^{B_{M2}} - 1] \}, \quad \alpha_s > \alpha_{sI}, \quad (28)$$

$$p_s = 0.0, \quad \alpha_s < \alpha_{sI}$$

and the constants are fitted as follows:

Table 2: Parameters for Refitted Solids-Pressure Model

Parameter	Model III value
α_{sI}	0.580769002438
C_{M2}	6892700 (Pa)
A_{M1}	4.3634398407e-5
B_{M1}	38.072977270364
A_{M2}	4.41475836547218
B_{M2}	7.14454835369866

Solids pressure predictions from this model are shown in Figure 2.

2.3. Interchange Terms

Momentum transfer between the fluid and solids phases is modeled using classical Stokes / Ergun drag laws:

$$S_{\text{mom},i} = \rho_s \alpha_s C_{\text{drag}} (u_{f,i} - u_{s,i}), \quad (29)$$

For $\alpha_f > 0.8$, a Stokes model is used:

$$C_{\text{drag}} = \frac{3}{4} C_{\text{drv}} \frac{\rho_f \alpha_f^{-2.65}}{\rho_s d_p}, \quad (30)$$

with

$$C_{\text{drv}} = \frac{24 \mu_f}{\rho_f \alpha_f d_p} [1 + 0.15 \left(\frac{\rho_f \alpha_f d_p |\vec{V}_f - \vec{V}_s|}{\mu_f} \right)^{0.687}], \quad \frac{\rho_f \alpha_f d_p |\vec{V}_f - \vec{V}_s|}{\mu_f} < 1000 \quad (31)$$

$$C_{\text{drv}} = 0.44 |\vec{V}_f - \vec{V}_s|, \quad \frac{\rho_f \alpha_f d_p |\vec{V}_f - \vec{V}_s|}{\mu_f} > 1000$$

For $\alpha_f < 0.8$, an Ergun model is used:

$$C_{\text{drag}} = \frac{1}{\rho_s \alpha_f} \left[150 \frac{\alpha_s \mu_f}{\alpha_r d_p^2} + 1.75 \rho_f \frac{|\vec{V}_f - \vec{V}_s|}{d_p} \right] \quad (32)$$

In these expressions, the relative velocity magnitude is given as $|\vec{V}_f - \vec{V}_s| = \sqrt{(u_{f,i} - u_{s,i})(u_{f,i} - u_{s,i})}$.

Energy transfer between the fluid and solids phases is modeled by using a simple relaxation approach:

$$\rho_s \alpha_s C_{p,s} \left(\frac{\partial T_s}{\partial t} + u_{j,s} \frac{\partial u_{i,s}}{\partial x_j} \right) = S_{\text{energy}} = \frac{6 \alpha_s}{d_p^2} k_f N_u (T - T_p) \quad (33)$$

In this equation, the specific heat for sand (J/kg-K) is curve-fitted as

$$\begin{aligned} C_{p,s} &= a_{s1} + a_{s2} T_p + a_{s3} T_p^2 + a_{s4} T_p^3 + a_{s5} T_p^4, \\ a_{s1} &= -1.367634 \times 10^2 \\ a_{s2} &= 3.950952 \\ a_{s3} &= -4.941694 \times 10^{-3} \\ a_{s4} &= 2.868886 \times 10^{-6} \\ a_{s5} &= -6.188417 \times 10^{-10} \end{aligned} \quad (34)$$

This curve fit is valid for temperatures between 300 and 1600 K. For temperatures below 300 K, the specific heat is fixed as 674.7 J/kg-K, and for temperatures above 1600 K, the specific heat is fixed as 1230 J/kg-K. In Eq. (33), k_f is the thermal conductivity of the fluid phase, and the Nusselt number is expressed as a function of the solids voidage and relative velocity as

$$Nu = (7 - 10\alpha_f + 5\alpha_f^2)(1 + 0.7 \text{Re}^{0.2} \text{Pr}^{1/3}) + (1.33 - 2.4\alpha_f + 1.2\alpha_f^2) \text{Re}^{0.7} \text{Pr}^{1/3},$$

$$\text{Re} = \frac{\rho_f |\vec{V}_s - \vec{V}_f| d_p}{\mu_f}, \quad \text{Pr} = 0.72 \quad (35)$$

3. Numerical Methods

3.1. Eigenvalue Analysis

To arrive at an efficient method for solving the system of equations shown above, we reformulate the inviscid components of the equation set in a non-conservative form and then add artificial time derivatives of fluid and solids pressure to the continuity equations for each phase. Writing this system in a quasi-linear, one-dimensional form for convenience, we have the following:

$$M \frac{\partial V}{\partial t} + A \frac{\partial V}{\partial x} = 0, \quad (36)$$

where

$$V^T = [Y_v, \alpha_f, u_s, u_f, p, T] \quad (37)$$

and

$$M = \begin{pmatrix} \rho_f \alpha_f & 0 & 0 & 0 & 0 & 0 \\ 0 & -\rho_s(1 + \theta_s a_s^2) & 0 & 0 & 0 & 0 \\ 0 & 0 & \rho_s \alpha_s & 0 & 0 & 0 \\ 0 & 0 & 0 & \rho_f \alpha_f & 0 & 0 \\ \alpha_f \rho_f \Big|_{Y_v} & \rho_f & 0 & 0 & \alpha_f(\rho_f \Big|_p + \theta_f) & \alpha_f \rho_f \Big|_T \\ \rho_f \alpha_f h_f \Big|_{Y_v} & 0 & 0 & \rho_f \alpha_f u_f & \rho_f \alpha_f h_f \Big|_p - \alpha_f & \rho_f \alpha_f h_f \Big|_T \end{pmatrix},$$

$$A = \begin{pmatrix} \rho_f \alpha_f u_f & 0 & 0 & 0 & 0 & 0 \\ 0 & -\rho_s u_s & \rho_s \alpha_s & 0 & 0 & 0 \\ 0 & -\rho_s a_s^2 & \rho_s \alpha_s u_s & 0 & 0 & 0 \\ 0 & 0 & 0 & \rho_f \alpha_f u_f & \alpha_f & 0 \\ \alpha_f u_f \rho_f \Big|_{Y_v} & \rho_f u_f & 0 & \rho_f \alpha_f & \alpha_f u_f \rho_f \Big|_p & \alpha_f u_f \rho_f \Big|_T \\ \rho_f \alpha_f u_f h_f \Big|_{Y_v} & 0 & 0 & \rho_f \alpha_f u_f^2 & \rho_f \alpha_f u_f h_f \Big|_p & \rho_f \alpha_f u_f h_f \Big|_T \end{pmatrix} \quad (38)$$

The proper specification of the parameters θ_f and θ_s should allow control over the variation of the eigenvalues (characteristic speeds) of the system. The inclusion of the solids energy equation does not change the eigenvalues and thus it is omitted from the analysis. Also, it should be noted that the inclusion of the fluid pressure $-\alpha_s \frac{\partial p}{\partial x_i}$ term in the solids momentum equation renders the system non-

hyperbolic in time and greatly complicates the analysis. As such, this term is considered to be a source term for purposes of determining the characteristic speeds, which are the eigenvalues of $M^{-1}A$. After much manipulation, the characteristic polynomial may be written as follows:

$$P(\lambda) = [u_f - \lambda]^2 [(u_f - \lambda)(\frac{u_f}{a_f^2 \theta_f + 1} - \lambda) - \frac{a_f^2}{a_f^2 \theta_f + 1}] [(u_s - \lambda)(\frac{u_s}{a_s^2 \theta_s + 1} - \lambda) - \frac{a_s^2}{a_s^2 \theta_s + 1}] \quad (39)$$

with

$$a_s^2 = \frac{1}{\rho_s} \frac{\partial p_s}{\partial \alpha_s} \quad (40)$$

and

$$a_f^2 = \frac{\rho_f h_f|_T}{\rho_f \rho_f|_p h_f|_T - \rho_f|_T (\rho_f h_f|_p - 1)} \quad (41)$$

Let $\theta_f = \frac{1}{V_{R,f}^2} - \frac{1}{a_f^2}$ and $\theta_s = \frac{1}{V_{R,s}^2} - \frac{1}{a_s^2}$, where $V_{R,f}$ and $V_{R,s}$ are reference velocities for the fluid and solids phases. With these definitions, the eigenvalues may be found as

$$\lambda = u_f, u_f, \frac{1}{2}[u_f(1+M_{R,f}^2) \pm \sqrt{u_f(1-M_{R,f}^2)^2 + 4V_{R,f}^2}], \quad \frac{1}{2}[u_s(1+M_{R,s}^2) \pm \sqrt{u_s(1-M_{R,s}^2)^2 + 4V_{R,s}^2}] \quad (42)$$

where the reference Mach numbers are defined as $M_{R,f}^2 = \frac{V_{R,f}^2}{a_f^2}$ and $M_{R,s}^2 = \frac{V_{R,s}^2}{a_s^2}$. The common practice

in a preconditioning method of this type [21-23] is to choose

$$\begin{aligned} V_{R,f}^2 &= \min[\max(u_f^2, U_R^2), a_f^2] \\ V_{R,s}^2 &= \min[\max(u_s^2, U_R^2), a_s^2] \end{aligned} \quad (43)$$

This renders the characteristic speeds well conditioned at all flow speeds. Generalizing this development to wave propagation in the direction of a normal vector \vec{n} , we have

$$\begin{aligned} \lambda &= \vec{V}_f \cdot \vec{n}, \vec{V}_f \cdot \vec{n}, \frac{1}{2}[\vec{V}_f \cdot \vec{n}(1+M_{R,f}^2) \pm \sqrt{\vec{V}_f \cdot \vec{n}(1-M_{R,f}^2)^2 + 4V_{R,f}^2}], \\ &\vec{V}_s \cdot \vec{n}, \frac{1}{2}[\vec{V}_s \cdot \vec{n}(1+M_{R,s}^2) \pm \sqrt{\vec{V}_s \cdot \vec{n}(1-M_{R,s}^2)^2 + 4V_{R,s}^2}] \end{aligned} \quad (44)$$

It should be noted that one can consider the non-Newtonian part of the granular stress tensor in the eigenvalue analysis. In this case, the sound speed also has a directional dependence:

$$a_s^2 = \frac{1}{\rho_s} \frac{\partial p_s}{\partial \alpha_s} \left(1 - \frac{\sin(\phi) S_{ij} n_i n_j}{\sqrt{S : S + \varepsilon / d_p^2}} \right), \quad (45)$$

where n_i are the elements of the normal vector \vec{n} . This definition may be used in the finite-volume upwinding methods discussed next by associating the normal vector with that pointing outward from a cell face.

3.2. Low Diffusion Flux-Splitting Methods

In this work, we extend upwinding techniques previously developed for isothermal gas-solid flows in [7,8] to the present multi-phase system. Considering again one-dimensional flow for simplicity, we first define a ‘numerical speed of sound’ at a cell interface:

$$\tilde{a}_{f,1/2} = \left(\frac{\sqrt{u_f^2(1-M_{R,f}^2)^2 + 4V_{R,f}^2}}{1+M_{R,f}^2} \right)_{1/2} \quad (46)$$

where the $\frac{1}{2}$ notation indicates the evaluation of Eq. (46) using cell-averaged velocity and sound-speed data. Other quantities needed in the formulation are Mach numbers at left (L) and right (R) states:

$$M_{L/R} = \frac{u_{f,L/R}}{\tilde{a}_{f,1/2}} \quad (47)$$

and Van Leer / Liou polynomials in Mach number:

$$\begin{aligned} M_{(1)}^\pm &= \frac{1}{2}(M \pm |M|), \\ M_{(2)}^\pm &= \begin{cases} \pm \frac{1}{4}(M \pm 1)^2, & |M| < 1 \\ M_{(1)}^\pm, & |M| > 1 \end{cases} \end{aligned} \quad (48)$$

Given these basic definitions, the convective and pressure portions of the interface flux are expressed as:

$$\begin{aligned} F_{f,1/2}^c &= \rho_{f,L} \alpha_{f,L} U^+ \phi_L + \rho_{f,R} \alpha_{f,R} U^- \phi_r, \\ F_{f,1/2}^p &= P_{f,1/2} \Psi \end{aligned}, \quad (49)$$

with

$$\begin{aligned} \phi &= [Y_v, 1, u_f, H_f]^T, \\ \Psi &= [0, 0, 1, 0]^T \end{aligned} \quad (50)$$

The split velocities U^\pm and interface pressure $P_{f,1/2}$ are defined as follows:

$$\begin{aligned} U^+ &= \tilde{a}_{f,1/2} [M_{(2),L}^+ - M_{1/2} (1 - \frac{\Delta p + |\Delta p|}{2\rho_{f,L} V_{R,f,1/2}^2})], \\ U^- &= \tilde{a}_{f,1/2} [M_{(2),R}^- + M_{1/2} (1 + \frac{\Delta p - |\Delta p|}{2\rho_{f,R} V_{R,f,1/2}^2})], \\ P_{f,1/2} &= \frac{1}{2} (p_L + p_R) + \frac{1}{2} (P^+ - P^-) (p_L - p_R) + \rho_{f,1/2} V_{R,f,1/2}^2 (P^+ + P^- - 1) \end{aligned} \quad (51)$$

where $\Delta p = p_L - p_R$. The function $M_{1/2}$ is given as

$$M_{1/2} = \frac{1}{2} (M_{(2),L}^+ - M_{(1),L}^+ - M_{(2),R}^+ + M_{(1),R}^+) \quad (52)$$

and the Mach number functionals used in the interface pressure definition are given as

$$P^\pm = \begin{cases} \frac{1}{2}(1 \pm M), & |M| < 1 \\ \frac{1}{M} M_{(1)}^\pm, & |M| > 1 \end{cases} \quad (53)$$

Discretization of the solids continuity term and the interface solids pressure follows in a similar manner. The ‘numerical speed of sound’ for the solids phase is defined as

$$\tilde{a}_{s,1/2} = \left(\frac{\sqrt{u_s^2(1-M_{R,s}^2)^2 + 4V_{R,s}^2}}{1+M_{R,s}^2} \right)_{1/2} \quad (54)$$

and the interface Mach numbers and Mach-number functionals (Eqs. (47), (48), and (52)) are redefined using the solids sound speed a_s and the solids velocity u_s . The convective flux in the solids continuity equation and the interface solids pressure then become:

$$\begin{aligned} F_{s,1/2}^c \Big|_{\text{cont}} &= \rho_{s,L} \alpha_{s,L} U^+ + \rho_{s,R} \alpha_{s,R} U^-, \\ F_{s,1/2}^P &= P_{s,1/2} \Psi \end{aligned} \quad (55)$$

The split velocities U^\pm and interface pressure $P_{s,1/2}$ are re-defined as:

$$\begin{aligned} U^+ &= \tilde{a}_{s,1/2} [M_{(2),L}^+ - M_{1/2} (1 - \frac{\Delta p_s + |\Delta p_s|}{2 \rho_{s,L} \alpha_{s,L} V_{R,f,1/2}^2})], \\ U^- &= \tilde{a}_{s,1/2} [M_{(2),R}^- + M_{1/2} (1 + \frac{\Delta p_s - |\Delta p_s|}{2 \rho_{f,R} \alpha_{s,R} V_{R,s,1/2}^2})], \\ P_{f,1/2} &= \frac{1}{2} (p_{s,L} + p_{s,R}) + \frac{1}{2} (P^+ - P^-) (p_{s,L} - p_{s,R}) + \rho_{s,1/2} \alpha_{s,1/2} V_{R,f,1/2}^2 (P^+ + P^- - 1) \end{aligned} \quad (56)$$

There are some differences in the split velocity and interface pressure definitions for the fluid and solids phases. In the fluid-phase forms, the pressure diffusion terms in the continuity equation are multiplied by α_f so that in the limit of compaction to a solid state, the convective fluid flux vanishes. The solids pressure terms naturally vanish in the limit that α_s goes to zero, so there is no need to multiply the pressure diffusion terms in the solids continuity equation again by α_s . The interface pressure definition for the fluid phase does not depend on the volume fraction, as the entire pressure gradient will vanish as α_f goes to zero. For the solids phase, it is necessary that each term in the interface pressure definition vanish as α_s goes to zero, and as such, the velocity diffusion term in Eq. (56) must be multiplied by α_s .

3.3. Time Integration Scheme

The three-phase Navier-Stokes system described above is implemented into a version of REACTMB-MP, a general purpose Navier-Stokes solver for multi-phase, multi-component flows developed at North Carolina State University. The governing equations are discretized in a cell-centered finite-volume manner, with the LDFSS formulation described above used for the inviscid fluxes. Slope limited total-variation diminishing (TVD) variable-extrapolation techniques are used to extend LDFSS to second-order accuracy for most of the calculations. One set of calculations for water entry uses the 4th order accurate Piecewise Parabolic Method (PPM) [24] in place of the TVD scheme. Time integration is facilitated by a planar relaxation sub-iteration procedure which results in second-order temporal accuracy with sufficient sub-iteration convergence. For steady-state problems, local time-stepping is used to accelerate convergence. The code is written to handle simply-connected, multi-block meshes and is parallelized using domain-decomposition / MPI message-passing methods. To formulate components of the stress tensor at cell interfaces, we require gradients evaluated at the interfaces. Given a cell interface $i+1/2$, we first define the vector pointing from cell-centers i to $i+1$ as

$$\vec{\tau} = (x_{i+1} - x_i) \hat{i} + (y_{i+1} - y_i) \hat{j} + (z_{i+1} - z_i) \hat{k} \quad (57)$$

then calculate the gradient of any quantity ϕ at the cell interface by

$$\nabla \phi = [\overline{\nabla \phi} - (\overline{\nabla \phi} \cdot \frac{\vec{\tau}}{|\vec{\tau}|}) \frac{\vec{\tau}}{|\vec{\tau}|}] + \frac{(\phi_{i+1} - \phi_i)}{|\vec{\tau}|} \frac{\vec{\tau}}{|\vec{\tau}|}, \quad (58)$$

where

$$\overline{\nabla \phi} = \frac{1}{2}(\nabla \phi_i + \nabla \phi_{i+1}) \quad (59)$$

Gradients at cell centers are calculated using standard Green-Gauss techniques. The splitting of the gradient vector into a component aligned with $\bar{\tau}$ and one perpendicular to $\bar{\tau}$ helps to maintain smooth solutions.

3.4. Arbitrary Lagrangian-Eulerian (ALE) Formulation

To account for projectile deceleration due to hydrodynamic forces, we have adopted an Arbitrary Lagrangian-Eulerian (ALE) framework [25-27]. In this, a reference frame attached to the projectile is allowed to move at speeds dictated by the solution of Newton's laws of motion:

$$\begin{aligned} \frac{dx_p}{dt} &= u_p, \\ m_p \frac{du_p}{dt} &= \sum F_x \end{aligned} \quad (60)$$

Integration of these equations at each time step provides the new position of the center of mass of the projectile (x_p), referenced to a datum line fixed at the water-air or sand-air interface, and the new velocity (u_p), which is used as a fixed grid speed in the ALE formulation. Velocity components are measured with respect to this reference frame. This requires some modifications to the interface fluxes and Jacobian elements, as discussed in [26] and [27]. Though the ALE formulation generalizes to three dimensions, only rectilinear deceleration is considered in this paper.

3.5. Overset Mesh Framework

Economical, accurate simulations of the dynamic entry of a projectile into different substrates requires some means of resolving the flowfield around the body while accounting for the long distances (relative to the penetrator size) that must be traversed before the projectile stops. Forces and moments generated on the projectile may result in deviations from the initial path, and it is necessary that the computational grid follow the motion of the projectile. The overset mesh approach [28,9,10] is one of the more powerful techniques available to handle such situations. In overset meshing, a background mesh with coarser spatial resolution is constructed for the entire computational domain. Local meshes which may move relative to the background mesh are generated around the projectile. Flow solutions within the background and local meshes are time-advanced in tandem, and the solutions are transferred among the meshes using interpolation procedures. The recent development of automatic C-language libraries for facilitating this information transfer [9,10] has greatly simplified the addition of an overset mesh procedure into computational codes. The SUGGAR code starts with an assembly of overset meshes, determines which meshes lie inside one another, cuts holes in the overlying meshes, and determines interpolation stencils for transferring information from one mesh to another. The DiRTLIB routine uses information from SUGGAR to construct local communication routines that facilitate the information transfer. The DiRTLIB routines link with the main CFD code in a straightforward fashion, only requiring such information as the set of flow variables and the array sizes. Communication (through MPI) is done separately from the normal inter-block communication used in the code. "Blanked out" regions in a computational domain, corresponding to parts of the flow that are solved on other meshes, are handled using an IBLANK array, which forces the code not to update the fluid properties when IBLANK is one. The SUGGAR code is written to be used with meshes that

generally overlap one another, as opposed to the simply connected, non-overlapping meshes used in our calculations. A significant amount of time was spent in working with SUGGAR to enable it to correctly respond to background and local meshes that themselves were composed of non-overlapping meshes. The solution involves incorporating details of the block-to-block connectivity into SUGGAR's input deck. This is a time-consuming task for meshes with large numbers of blocks, and SUGGAR's format does not account for complex inter-connections among mesh blocks that might occur in practice. Future work will require the development of software that automatically performs a translation between our connectivity format and that required by SUGGAR. Figure 3 presents two overset meshes, one of which uses a set of overlapping meshes for the background mesh and the other which uses a set of simply-connected meshes. The topology of the composite mesh is rendered reasonably well in both cases, but the holes are cut in clearly different ways.

3.6. Sharp Interface Capturing

To account for wave breakage effects during water penetration and for precise estimation of loads encountered during water cavity inception and collapse, it is necessary that the discretization scheme capture phase interfaces in as few cells as possible. This can be accomplished by blending the baseline higher-order scheme (TVD or PPM) with a bounded downwind differencing scheme, such as THINC [29] or CICSAM [30]. THINC (Tangent of Hyperbola Interface Capturing) uses the tangent hyperbola function as a model function for a discontinuous volume (or mass) fraction within a mesh cell. The average volume fraction at cell i is defined as

$$\bar{\alpha}_i = \frac{1}{\Delta x_i} \int_{x_{i-1/2}}^{x_{i+1/2}} \frac{\varepsilon}{2} [1 + \gamma \tanh(\beta(\frac{x - x_{i-1/2}}{\Delta x_i} - \tilde{x}_i))] dx, \quad (61)$$

where ε , γ , and β are parameters that control the sharpness of the approximation and its connection with cell-averaged information at neighboring cells. The location of the center of the distribution \tilde{x}_i is determined by enforcing the equality in Eq. (61), given the other parameters. Other model functions can be used – a linear distribution may be represented as

$$\begin{aligned} \bar{\alpha}_i &= \frac{1}{\Delta x_i} \int_{x_{i-1/2}}^{x_{i+1/2}} \frac{1}{2} [1 - \gamma + 2\gamma \bar{x}] dx, \\ \bar{x} &= \max[0, \min[1, \frac{x - x_{i-1/2}}{\Delta x_i} - \tilde{x}_i]] \end{aligned}, \quad (62)$$

where again, \tilde{x}_i is determined by enforcing the equality in Eq. (62). It is clear that this framework is directly consistent with TVD or PPM -type interpolation methods in that left- and right-state information may be obtained easily from the assumed form for the discontinuity within a cell. These techniques tend to always sharpen gradients, and in some cases, this can lead to unphysical ‘stair-stepped’ interface profiles and the shedding of spurious pockets of material (known as ‘flotsam’ and ‘jetsam’ in the literature). To avoid this behavior, one can blend the baseline TVD or PPM scheme with a sharp-interface scheme using a linear weighting procedure. In the CICSAM scheme [30], the weighting parameter W at a cell interface is a function of the angle between the captured phase interface and the normal vector to the mesh-cell interface ($W = W(\frac{\nabla \alpha \cdot \vec{n}}{|\nabla \alpha|})$), and if the angle

approaches ninety degrees, the method shifts to the sharp-interface capturing strategy. Our tests have shown that this procedure works well on uniform meshes, but on the highly stretched meshes necessary to capture viscous layer development on the projectile surfaces, the method leads to oscillations. As

such, we have implemented an alternative weighting that considers not only the direction of the phase interface but also the magnitude of the gradient:

$$W = W \left(\frac{|\nabla \alpha \cdot \vec{n}|}{|\nabla \alpha \cdot \vec{n}| + \frac{\varepsilon}{\Delta}} \right), \quad (63)$$

where ε / Δ is a cut-off minimum gradient. An advantage of this form is that the sharp-interface contribution will be diminished as the gradient becomes small, relative to the cutoff, even if the phase interface is parallel to the cell interface. This should allow a more realistic representation of two-phase mixing processes that may not be discontinuous at the mesh scale.

3.7. Grid Arrangement

Three projectile configurations are considered in this work. Closeup views of some of the axisymmetric grids are shown in Figure 4. Configuration I (Figure 4a) is a generic dart shape representative of those used in beach / surf-zone clearance applications. Configuration II (Figure 4b) corresponds to one of the ballistic shapes (Round 10) considered in an early investigation of projectile penetration into dry sand. [31,32] Configuration III (Figure 4c) was used in sand-penetration tests conducted by Lockheed Martin. [33] Table 3 summarizes the total number of interior mesh cells and blocks in each grid. Also listed are specifics for two additional renderings of Configuration III – one three-dimensional and the other axisymmetric with overset meshes (see Figure 3).

Table 3: Grid Configurations and Data

Configuration	cells	blocks
I	78973	16
II	48948	28
III	20947	20
III-C (3-D)	678034	48
III-D (overset)	34760 (projectile) 25032 or 5376 (background)	29

4. Results

4.1. Water Entry

The first set of results focuses strictly on the entry of an axisymmetric projectile into water. The granular-flow model is not utilized in these calculations. Figure 5 presents drag and drag coefficient versus depth for dart entry (Configuration I) into water. A dramatic increase in drag is noted as the dart first enters the water and a cavity is established. From this point, the drag decreases steadily as a supercavity is formed. Neaves and Edwards [1] simulated this case using a supercavitation code developed at NSWC-PC. The results presented are in good agreement with the earlier ones. The use of a finer grid in the current calculations does result in a narrower region of peak drag, as the water / air interface is captured more sharply.

Figure 6 shows snapshots of the flowfield about the nose (top sequence) and tail (bottom sequence) for a dart (Configuration I) undergoing deceleration in water. The right side of each figure is the bulk fluid

density while the left side is the pressure. Initially, the water is at 420 m/s and the dart is completely contained within the cavity. As the dart decelerates, the cavity eventually collapses behind the dart and moves forward along the body. This case illustrates the ability of the ALE formulation to account for this time-dependent dart response. Figures 7 and 8 present drag coefficient versus time and dart velocity versus depth. Deviations from analytical results obtained assuming a constant drag coefficient are noted as the dart velocity decelerates below 80 m/s. An initial decrease in drag coefficient occurs as the cavity first collapses to the dart trailing edge but the drag coefficient then rises as the back of the projectile becomes more wetted.

Figure 9 shows an example of the use of sharp-interface capturing methods (Section 3.6) in simulating vertical entry of a dart into water. The dart geometry and initial speed are that of Configuration III and the refined projectile mesh [Configuration III-D in Table 3] is used without the background grid. The ALE formulation is not used. The snapshots compare, from left to right, solutions obtained using the PPM scheme without interface-sharpening, the THINC scheme (Eq. (61)) and the linear reconstruction scheme (Eq. (62)). The top set of snapshots shows the liquid water mass fraction, with the darker contours representing the water. The bottom set of snapshots shows the velocity field induced in the wake of the projectile. The thin lines represent the 10%, 50%, and 90% contours of water mass fraction. The solutions obtained using the sharp-interface capturing schemes show more fine-scale features, including secondary instabilities along the cavity interface that result from vortex interactions. The appearance of these features may be due to the fact that surface-tension effects are much better resolved when the sharp-interface capturing methods are used. The wake of the projectile is broader and more dynamic for the THINC and linear reconstruction methods.

4.2. Sand Entry – Configuration II

Figures 10 and 11 present results for steady flow of a sand /air mixture over the Configuration II projectile. [32,33] The ALE formulation is not used in this calculation, solids-pressure Model I is used, and the calculation is conducted in a non-time accurate manner using local time stepping. Conditions correspond to those encountered just after entry into the sand bed ($u_p = 742$ m/s, $\alpha_s = 0.614$). A steady solution is sought at these conditions to provide an initial estimate of the drag coefficient. Figure 10 presents solids voidage contours for two values of the assumed loading voidage α_{s0} but with the solids shear stress tensor omitted (ϕ in Eq. (15) set to 0). The sand is compacted at the nose of the projectile to a voidage of around 0.825 in both cases, and a large cavity filled with air is formed as the granular mixture expands around the blunt nose of the projectile. A shock front forms ahead of the projectile and reflects from the upper wall of the container. This front is associated with the onset of compaction, which raises the sound speed of the granular material to levels comparable to the fluid velocity. There is little difference in the solutions for the two choices of α_{s0} . More substantial differences are shown in Figure 11, which illustrates the effect of including the solids shear stresses (with $\phi=28$ degrees). The bow shock angle is not changed substantially, but the location of the air/sand interface shifts toward the surface when shear stresses are included. Some striations in the interface downstream of the end of the projectile are observed. These tend to persist over the iteration sequence, precluding good steady-state convergence. The inclusion of the shear-stress terms, while not destabilizing, does not always yield smooth solutions for volume fraction and solids pressure. At the nose, the solids pressure reaches a maximum value of $5.7\text{e}8$ Pa for the case with no shear stresses, as compared with local values of up to $7.8\text{e}8$ Pa for the case including shear stresses. Figure 12 shows projectile velocity versus depth and time for the experiment. This data can be regressed to yield an

effective drag coefficient C_d of 2.02. Table 4 indicates that the calculations predict a value of about half of the experimental value and that the inclusion of shear-stress terms slightly increases the average drag coefficient. The drag coefficient including shear stresses does not stabilize at a constant value but oscillates between values of about 1.13 and 1.35. Due to the formation of the cavity, the drag force is due almost exclusively to the solids pressure acting on the projectile nose, implying either that more compaction should occur under these conditions or that the modeled solids pressure is too low for the amount of compaction that is predicted to occur.

Table 4: Drag Predictions: Configuration II

Configuration	Measured C_d	Predicted C_d
II ($\alpha_{s0} = 0.614$, no solids shear stress)	2.02	1.050
II ($\alpha_{s0} = 0.64$, no solids shear stress)	2.02	1.045
II ($\alpha_{s0} = 0.614$, solids shear stress)	2.02	1.13-1.35

4.3. Sand Entry – Configuration III (Initial Results)

Initial results obtained for the Lockheed-Martin dart (Configuration III) are shown in Figures 13-15. Conditions again correspond to those just after entry into the sand bed ($u_p = 305$ m/s, $\alpha_s = 0.56$). Solids voidage contours in Figure 13 illustrate the effect of varying the voidage value (α_{s0}) at which the sand is assumed to begin elastic/plastic compression. Solids shear stresses are omitted in this case. Regions of strong compression of the sand, followed by the formation of a cavity filled with air, are indicated for both cases ($\alpha_{s0} = 0.56$ and $\alpha_{s0} = 0.6$). The onset of strong compression appears to be dictated by the Mach number based on the solids sound speed (shown in Figure 14). For the case where $\alpha_{s0} = 0.56$, corresponding to a partially loaded initial state, the solids sound speed is higher in the granular media and increases further due to compaction. The locations at which the solids velocity becomes lower than the solids sound speed define the upstream extent of the bow shock located in front of the projectile. The solids phase is initially unloaded when $\alpha_{s0} = 0.6$, the sound speed is extremely small, and some compression occurs before the sonic line is reached. The shock front is located closer to the body and curves more strongly downstream of the nose region.

Figure 15 shows the effect of including the solids shear stress tensor for $\alpha_{s0} = 0.56$. The dominant effect is to force the sand/air cavity interface closer to the body. This leads to partial “wetting” of the forebody section with sand and thus to a higher drag coefficient (see Table 5). Figure 16 shows experimental velocity versus depth data for two cases involving projectile penetration into sand. This data has been used to extract a drag coefficient of 1.03 for the initial stages of entry. Table 5 shows that again, the numerical approach underpredicts the drag coefficient. If sand contacts only the nose, then the predicted drag coefficient is around 0.21. The partially “wetted” case (including shear stress terms) shown in Figure 15 yields a drag coefficient of 0.472, but the same case with $\alpha_{s0} = 0.6$ (initially unloaded) yields a drag coefficient of only 0.264, as again, a full cavity is formed.

Table 5: Drag Predictions: Configuration III (Initial Results)

Configuration III	Measured C _d	Predicted C _d
$\alpha_{s,0} = 0.56$, no solids shear stress	1.03	0.220
$\alpha_{s,0} = 0.6$, no solids shear stress	1.03	0.213
$\alpha_{s,0} = 0.56$, solids shear stress	1.03	0.472
$\alpha_{s,0} = 0.6$, solids shear stress	1.03	0.264

4.4. Sand Entry – Configuration III (Later Results)

Much of the work performed after the publication of [34] focused on trying to determine the causes of the underprediction of the drag coefficient and on developing methods for improving the results. As a first step, a three-dimensional mesh was generated for one sixth of the Lockheed-Martin dart configuration (Configuration III-C in Table 3). The fins were included in the computational domain. Calculations of the three-dimensional flow using the same model as used in Sections 4.2 and 4.3 were performed with and without the granular shear-stress model. Figure 17 presents a snapshot of solids voidage contours for these cases. The fins do not penetrate the sand cavity interface in either case. The rotational flow induced by the fins entrains more sand into the wake of the projectile, and some sand is collected onto the flat leading edges of the fins. As shown in Table 6, the inclusion of three-dimensionality does not substantially improve predictions of the drag coefficient. Because of the expense of the calculations, work on the 3-D configuration was discontinued in order to focus on trade-off studies performed on the axisymmetric meshes.

The next step involved re-fitting the solids stress model based on Lockheed-Martin sand-compaction data (Model II in Section 2.2), which was not available prior to the publication of [34]. This change, along with the addition of a Newtonian regularization term to the solids-stress tensor (Section 2.2) and a more accurate formulation of the solids stress tensor at cell interfaces, yielded improved results for the drag coefficient (Table 6). Figure 18 shows contours of solids volume fraction obtained using the improved solids-stress model. The inclusion of solids shear stress effects forces the sand cavity interface closer to the body surface. This leads to more ‘wetting’ of the forebody section with sand and a higher drag coefficient. Even with these improvements, it became clear that only the complete wetting of the forebody section (up until the maximum cross-sectional area) would lead to a more correct prediction of the projectile drag coefficient, at least under axisymmetric, steady conditions.

Table 6: Drag Predictions: Configuration III (Later Results)

Configuration III (later results)	measured C _d	predicted C _d
$\alpha_{s,o} = 0.56$, no solids shear stress	1.03	0.220
$\alpha_{s,o} = 0.56$, no solids shear stress (3-D)	1.03	0.215
$\alpha_{s,o} = 0.56$, with solids shear stress (3-D)	1.03	0.360
$\alpha_{s,o} = 0.56$, with solids shear stress (original form presented in AIAA Paper 2006-1289)	1.03	0.472
$\alpha_{s,o} = 0.56$, with solids shear stress (new coding of solids stress tensor with regularization and with new fit to solids pressure (Figure 1))	1.03	0.668 (average)

4.5. Sand Entry – Configuration III-D

The latest results obtained for the Lockheed-Martin dart configuration have used a refined mesh (Configuration III-D) that eliminates the hollowed-out region at the end of the dart. The mesh was generated using less-severe stretching ratios and more mesh points per block in the hopes that the elements of the granular stress tensor would be resolved more correctly, thus providing improved steady state convergence and more accurate results. The latest runs also used the new solids-pressure model (Model III in Section 2.2), which was designed to produce a larger increase in the sound speed as one approaches a loaded state while maintaining a good fit to the Lockheed-Martin sand-compaction data. Several parametric studies were performed, varying such factors as the initial solids loading, the inclusion or non-inclusion of the direction-dependent sound speed (Eq. (45)) in the upwind method, the choice of the constant $C_{s,N}$ scaling the Newtonian viscosity component of Eq. (15), and the use of a ‘thin layer’ form of the solids-stress tensor that neglects the gradient components parallel to the \vec{r} direction. Table 7 summarizes some of the results of these parametric studies.

Table 7: Parametric Studies Performed on Configuration III-D

Case number (Configuration III-D)	$\alpha_{s,o}$	$C_{s,N}$	directional sound speed	thin layer form	predicted C_d (range)
1	0.56	0.00	no	no	0.529-0.543
2	0.56	0.00	yes	no	0.465-0.469
3	0.56	0.01	no	no	0.557-0.531
4	0.56	0.10	no	no	0.578-0.586
5	0.56	1.00	no	no	0.747-0.853
6	0.58	1.00	no	yes	0.740-0.810

Many other combinations of parameters were tried. In general, increasing the initial value of α_s toward the fitted value for the onset of compaction ($\alpha_{sl} = 0.580769002438$) led to increases in the drag coefficient, as did increases in $C_{s,N}$. In some cases, however, this response was accompanied by the destabilization of the cavity wake, initiated by large oscillations in the vicinity of the cavity inception point. Even when destabilization did not occur, convergence was very poor. A significant effort was undertaken to understand the causes of convergence degradation. It was found that it was a result, primarily, of oscillations in the solids properties in the vicinity of the projectile nose but that large drag terms, caused by a wide disparity in solids and fluid velocities in the projectile wake, also contributed to the response. Figure 19 shows a close-up view of solids volume fraction and pressure in the vicinity of the projectile nose for Case 5. The formation of the cavity is delayed until the maximum-area point, and the entire forebody of the projectile is ‘wetted’ by the sand.

4.6. Overset Mesh Results – Configuration III-D

As mentioned in Section 3.5, we were able to embed the computational model into an overset-mesh framework using the SUGGAR/DiRTLlib [9,10] utilities. We exercised this capability for a few cases, focusing primarily on ensuring that the procedures provided the correct information transfer between the projectile meshes and the background meshes. Figure 20 shows results obtained using SUGGAR / DiRTLlib for a case where the background meshes were allowed to overlap one another (bottom) and

for a case when the background meshes do not overlap (top). The solutions correspond to the meshes shown in Figure 3. The variable plotted is the transverse component of the solids velocity. The cases were run with different parameters, and close agreement between the solutions is not to be expected. The contours indicate that information is being passed correctly from one block set to another. The resolution differences between the background and projectile meshes lead to some smearing of the waves.

5. Conclusions

The development of a comprehensive three-phase model for simulating projectile penetration into water and sand has been outlined herein. The approach combines low-diffusion upwinding techniques valid for multi-phase flows with time-derivative preconditioning methods to ensure efficient, accurate time evolution at all speeds. The computational model has been embedded into an overset-mesh framework, which renders it suitable for eventual simulations of six-degree-of-freedom maneuver. Applications to supercavitating projectile entry into water and subsequent deceleration show good agreement with prior work and with experimental trends. Applications to situations representative of initial projectile entry into dry sand indicate that the current approach underpredicts measured drag coefficients by more than 75% in some cases. The addition of a solids pressure model that provides a sharper transition to a loaded state upon initial compaction and the inclusion of an *ad-hoc* Newtonian contribution to the baseline Mohr-Coulomb granular stress tensor results in better agreement with experimental data, with the best predictions for the drag coefficient being ~20% lower than the measurements. These results indicate that the current models for solids-stress (frictional) effects need to be improved. The assumption of axisymmetric flow may also be overly restrictive, as it is known that the motion such projectiles may exhibit sinuous and rotational modes accompanied by ‘tail slap’ on the walls of the cavity. Complete six-degree of freedom simulations of dynamic entry would therefore be required for a more complete analysis.

Publications

Neaves, M.D. and Edwards, J.R. “All-Speed Time-Accurate Underwater Projectile Calculations using a Preconditioning Algorithm”, *Journal of Fluids Engineering*, Vol. 128, No. 2, 2006, pp. 284-296

McDaniel, K.S., Edwards, J.R., and Neaves, M.D. “Simulation of Projectile Penetration into Water and Sand”. AIAA Paper 2006-1289, Presented at the 44th Aerospace Sciences Meeting and Exhibit, Reno, NV, January, 2006

Edwards, J.R.. “Computational Simulation of High-Speed Projectiles in Air, Water, and Sand” Final Report, Office of Naval Research Grant N000140510224, December, 2007.

Personnel

Jack R. Edwards, Principal Investigator

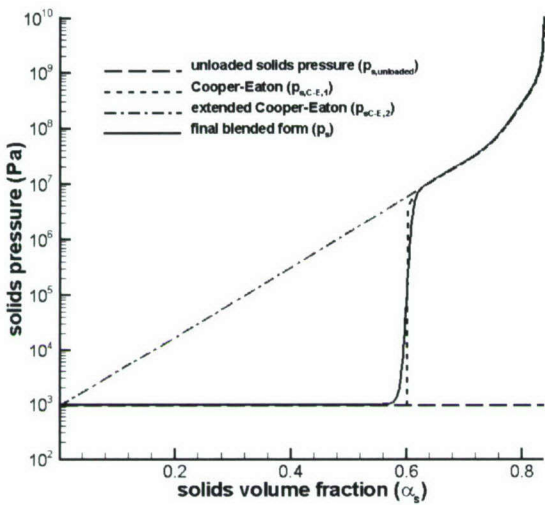
Keith McDaniel, Graduate Research Assistant (currently employed by Swales Aerospace in Hampton, Virginia but working toward completing his Ph.D)

This work was performed in collaboration with Dr. Michael D. Neaves, Naval Surface Warfare Center, Panama City, Florida.

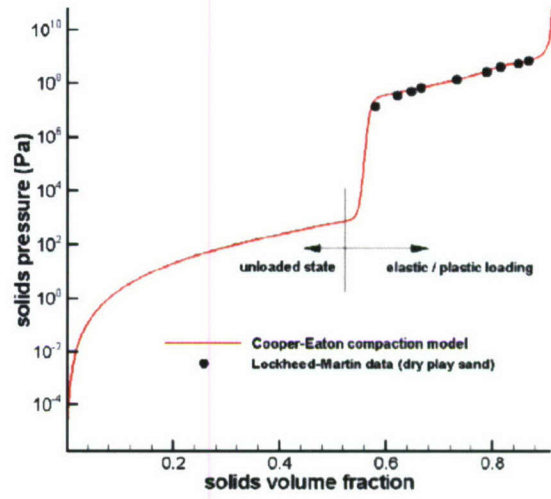
References

- [1] Neaves, M. D., and Edwards, J.R., "All-Speed Time-Accurate Underwater Projectile Calculations using a Preconditioning Algorithm", *ASME Journal of Fluids Engineering*, Vol. 128, No. 2, 2006, pp. 284-296
- [2] Neaves, M. D., and Edwards, J.R., "Time-Accurate Calculations of Axisymmetric Water Entry for a Supercavitating Projectile", 34th AIAA Fluid Dynamics Conference and Exhibit, Portland, Oregon, June, 2004. AIAA Paper 2004-2643.
- [3] Neaves, M. D., and Edwards, J.R., "Time-Accurate All-Speed Multiphase Calculations Using a Low-Diffusion Flux-Splitting Scheme", 42nd AIAA Aerospace Sciences Meeting & Exhibit, Reno, Nevada, January, 2004. AIAA Paper 2004-1282.
- [4] Neaves, M. D., and Edwards, J.R., "Hypervelocity Underwater Projectile Calculations Using a Preconditioning Algorithm", 41st AIAA Aerospace Sciences Meeting & Exhibit, Reno, Nevada, January, 2003. AIAA Paper 2003-1286.
- [5] Tian, M., Edwards, J.R., Lin, K.-C., and Jackson, T.A. "Numerical Simulation of Transient Two-Phase Flow within Aerated-Liquid Injectors," AIAA Paper 2003-4226,
- [6] Tian, M., Edwards, J.R., Lin, K.-C., and Jackson, T.A. "Numerical Simulation and Experimental Characterization of the Internal Two-Phase Flow within an Aerated-Liquid Injector" AIAA Paper 2004-2645.
- [7] Mao, D., Edwards, J.R., Kuznetsov, A.V., and Srivastava, R.K. "Development of Low-Diffusion Flux-Splitting Methods for Dense Gas-Solid Flows," *Journal of Computational Physics*, Vol. 185, No. 1, 2003, pp. 100-119.
- [8] Mao, D. and Edwards, J.R. "Simulation of Chemically-Reacting Gas-Solid Flows using a Preconditioning Strategy", AIAA Paper 2003-4110CP, June, 2003. *Chemical Engineering Science*. Vol. 59, No. 20, 2004, pp. 4279-4287.
- [9] Noack, R. "DiRTlib: A Library to Add an Overset Capability to Your Flow Solver," AIAA Paper 2005-5116.
- [10] Noack, R. "SUGGAR: A General Capability for Moving Body Overset Grid Assembly" AIAA Paper 2005-5117.
- [11] McBride, B.~J., Gordon, S., and Reno, M.~A., "Coefficients for Calculating Thermodynamic and Transport Properties of Individual Species", NASA TM-4513, October 1993.
- [12] Saurel, R. and Cocchi, J., "Numerical Study of Cavitation in the Wake of a Hypervelocity Underwater Projectile", *Journal of Propulsion and Power*, Vol. 15, No. 4, 1999, pp. 513-522.
- [13] Lide, D. (ed.), *Handbook of Chemistry and Physics*, 85th ed., Taylor and Francis, Boca Raton, Florida, 2005.
- [14] Schaeffer, D., "Instability in the Evolution Equations Describing Incompressible Granular Flow," *Journal of Differential Equations*, Vol. 66, 1987, pp. 19-50.
- [15] Tardos, G. "A Fluid Mechanistic Approach to Slow, Frictional Flow of Powders," *Powder Technology*, Vol. 92, 1997, pp. 61-74
- [16] Srivastava, A. "Analysis of a Frictional-Kinetic Model for Gas-Particle Flow" *Powder Technology*, Vol. 129, 2003, pp. 891-916.
- [17] Darteville, S., Numerical and Granulometric Approaches to Geophysical Granular Flows, PhD. Dissertation, Michigan Technological University, 2003.

- [18] Joseph, D. D. and Saut, J. C., "Short-Wave Instabilities and Ill-Posed Initial-Value Problems", *Theoretical and Computational Fluid Dynamics*, Vol. 1, pp.191-227, 1990.
- [19] Cooper, A. and Eaton, L. "Compaction Behavior of Several Ceramic Powders", *Journal of the American Ceramic Society*, Vol. 45, 1962, pp. 97-101
- [20] Kidwell, T., personal communication, Office of Naval Research , May, 2006.
- [21] Choi, Y.H. and Merkle, C.L. "The Application of Preconditioning in Viscous Flows" *Journal of Computational Physics*, Vol. 105, 1993, pp. 207-223.
- [22] Turkel, E. "Preconditioning Methods for Solving the Incompressible and Low Speed Compressible Equations," *Journal of Computational Physics*, Vol. 72, 1987, pp. 277-298.
- [23] Weiss, J.M. and Smith, W.A. "Preconditioning Applied to Variable and Constant Density Time-Accurate Flows on Unstructured Meshes," AIAA Paper 1994-2209, June, 1994.
- [24] Colella, P. and Woodward, P.R. "The Piecewise Parabolic Method (PPM) for Gas-Dynamical Simulations", *Journal of Computational Physics*, Vol. 54, pp. 174-201, 1984.
- [25] Hirt, C., Amsden, A., and Cook, H. "An Arbitrary Lagrangian-Eulerian Computing Method for all Flow Speeds" *Journal of Computational Physics*, Vol. 14, 1974, p. 227.
- [26] Smith, R. "AUSM(ALE): A Geometrically Conservative Arbitrary Lagrangian-Eulerian Flux-Splitting Scheme" *Journal of Computational Physics*, Vol. 150, 1999, pp. 268-286.
- [27] Neaves, M., McRae, D., and Edwards, J.R. "High-Speed Inlet Unstart Calculations Using an Implicit Solution-Adaptive Mesh Algorithm" AIAA Paper 2001-0825, January, 2001.
- [28] Buning, P.G., et al. "OVERFLOW User's Manual, Version 1.6ad. NASA Ames Research Center, March, 1993.
- [29] Xiao, F., Honma, Y., and Kono, T. "A Simple Algebraic Interface Capturing Scheme Using Hyperbolic Tangent Function" *International Journal of Numerical Methods in Fluids*, Vol. 48, 2005, pp.1023-1040.
- [30] Ubbink, O., and Issa, R.I. "A Method for Capturing Sharp Fluid Interfaces on Arbitrary Meshes" *Journal of Computational Physics*, Vol. 153, 1999, pp. 26-50.
- [31] Allen, W. A., Mayfield, E. B., Morrison, H. L. "The Dynamics of Projectile Penetration in Sand." U. S. Naval Ordnance Test Station, Research Department. NAVORD Report 4980. 1955.
- [32] Allen, W. A., Mayfield, E. B., Morrison, H. L. "The Drag Coefficient for Projectiles In Sand." U. S. Naval Ordnance Test Station, Research Department. NAVORD Report 5041. 1956.
- [33] Benedict, L., personal communication, Lockheed-Martin Corporation, December, 2005
- [34] McDaniel, K.S., Edwards, J.R., and Neaves, M.D. "Simulation of Projectile Penetration into Water and Sand" AIAA Paper 2006-1289, January, 2006.



a.) Model 1



b.) Model II

Figure 1: Solids pressure versus volume fraction for Cooper-Eaton Models I and II

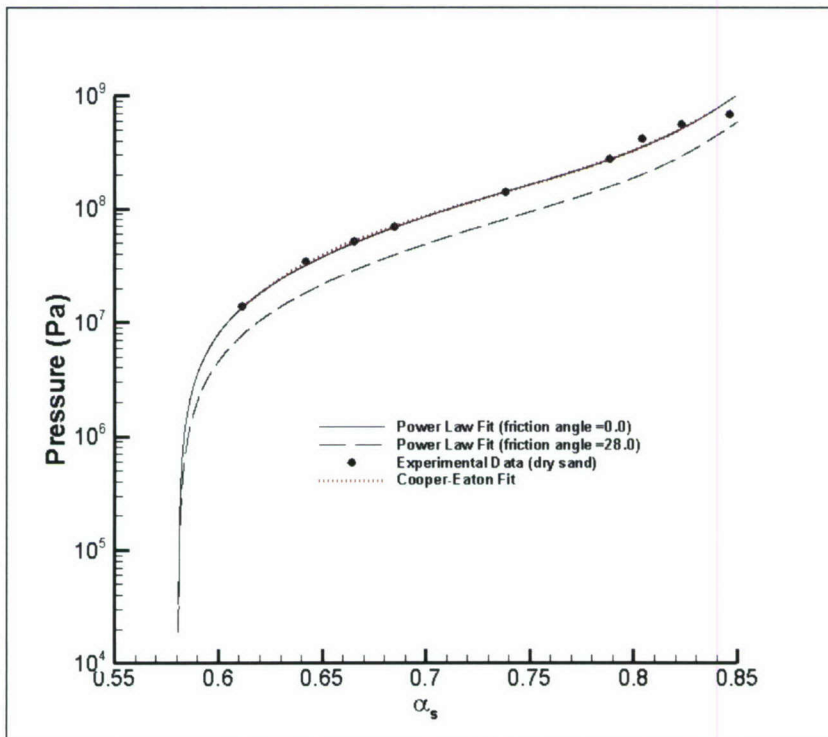


Figure 3: Solids pressure versus volume fraction for re-fitted Model III

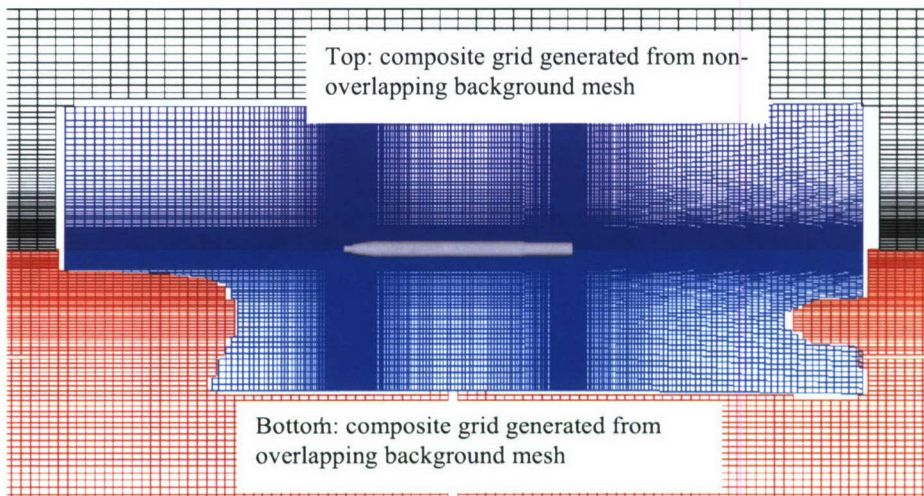


Figure 3: Composite grids generated by SUGGAR for overlapping and non-overlapping background meshes

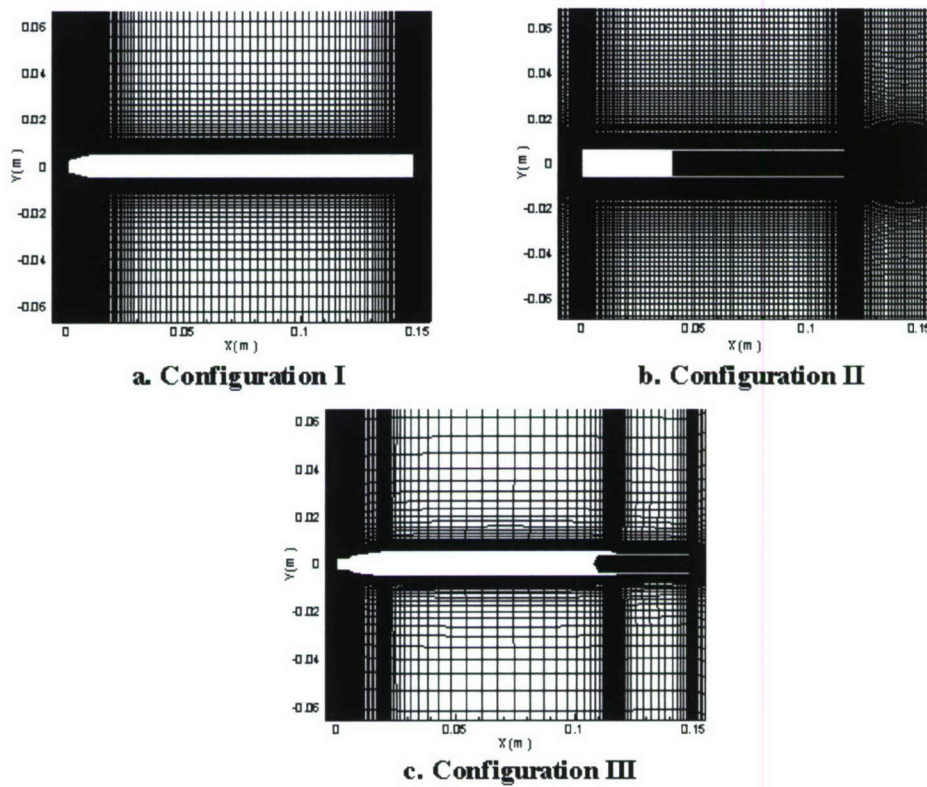


Figure 4: Grid details for projectile configurations (grid reflected about centerline for clarity)

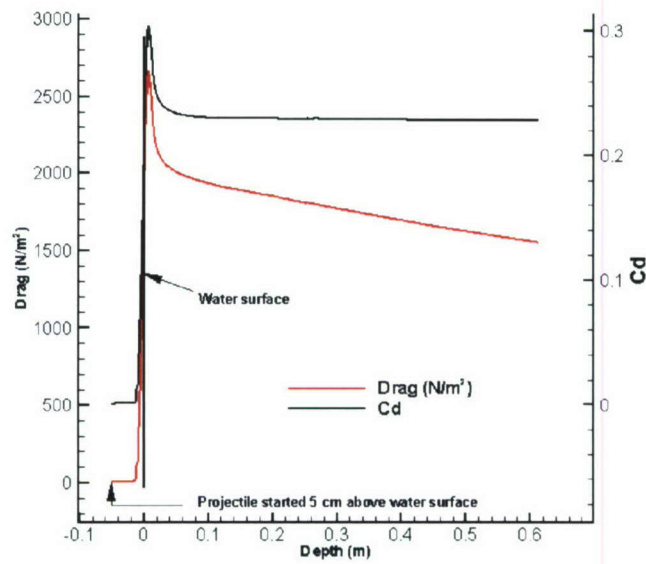


Figure 5: Drag and drag coefficient versus time for dart entry into water

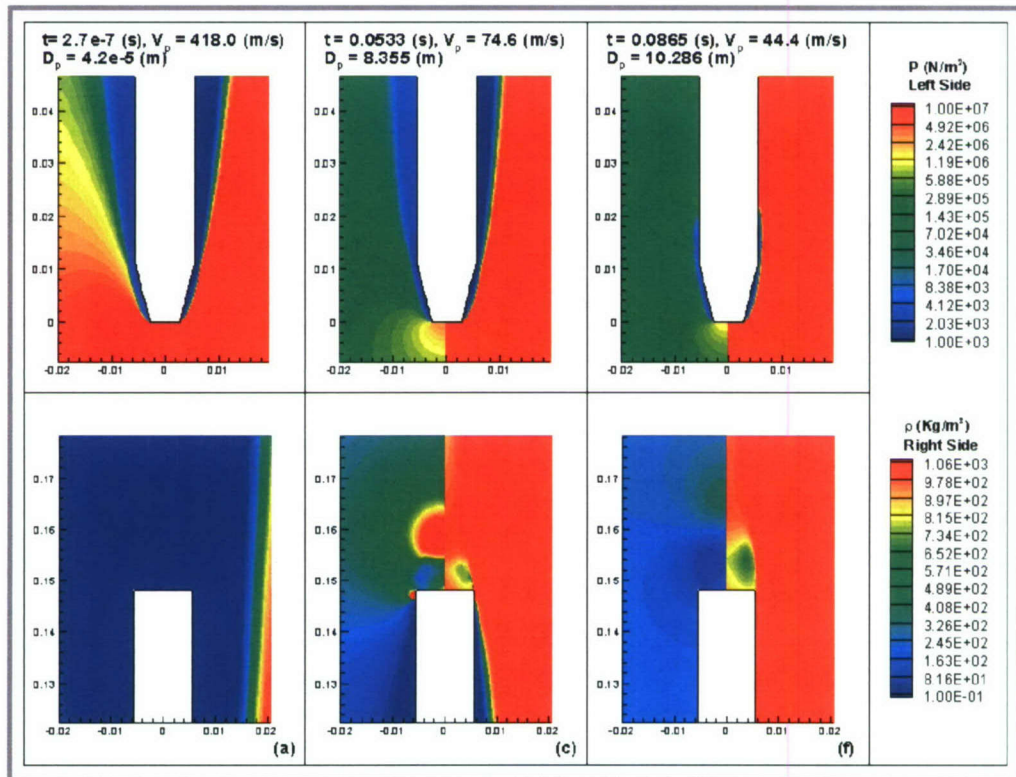


Figure 6: Snapshot of pressure and density contours: dart entry into water

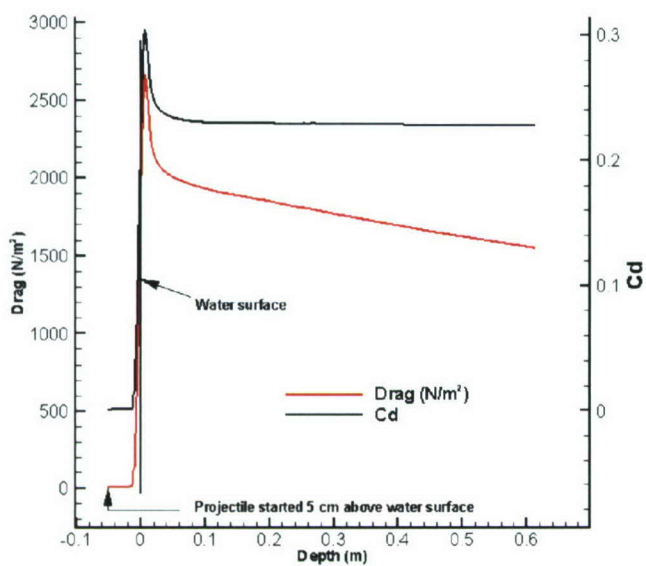


Figure 7: Drag coefficient versus time: dart deceleration in water

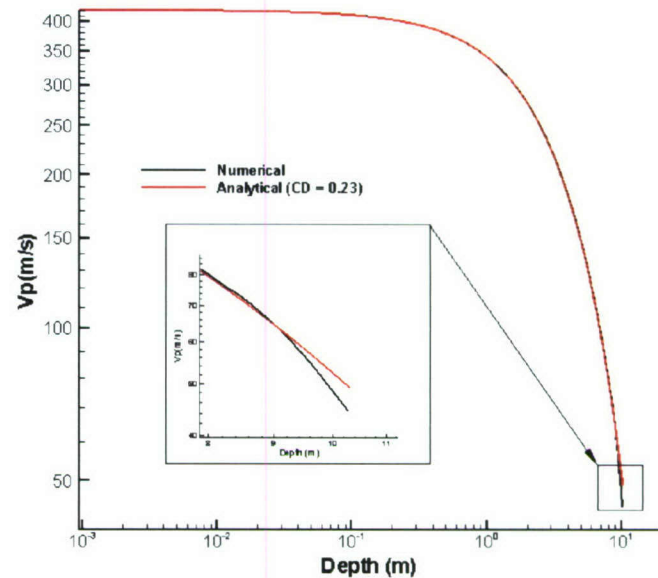


Figure 8: Velocity versus depth: dart deceleration in water

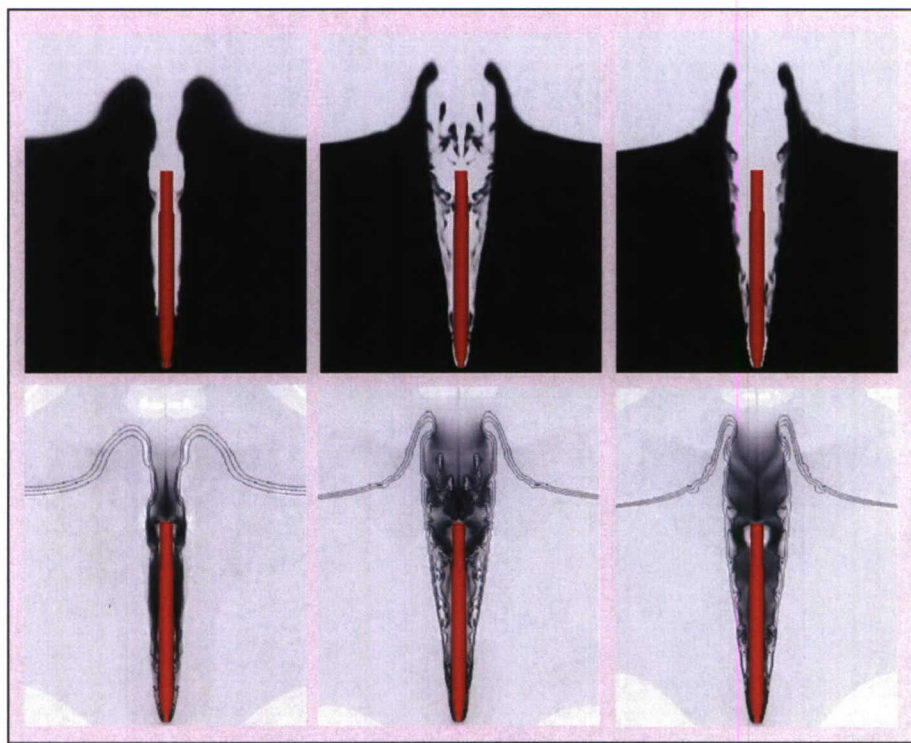


Figure 9: Predictions of vertical water entry using various interface-sharpening schemes (from left to right: PPM, PPM with THINC, PPM with linear reconstruction; top: water mass fraction; bottom: vertical velocity)

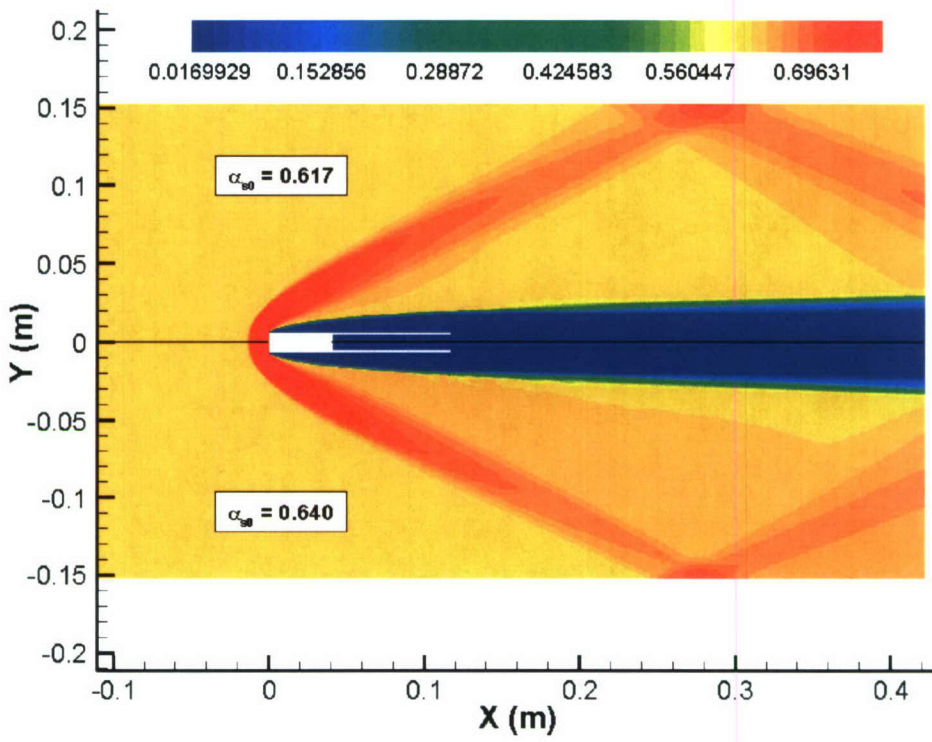


Figure 10: Solids voidage contours – effect of α_{s0} : Configuration II

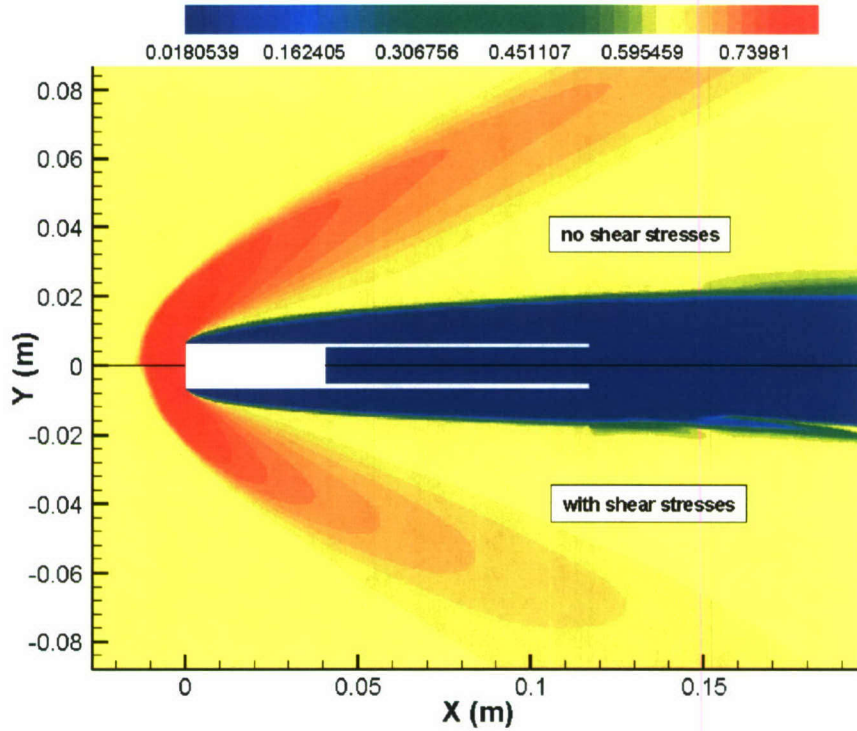


Figure 11: Solids voidage contours – effect of solids shear stresses:
Configuration II

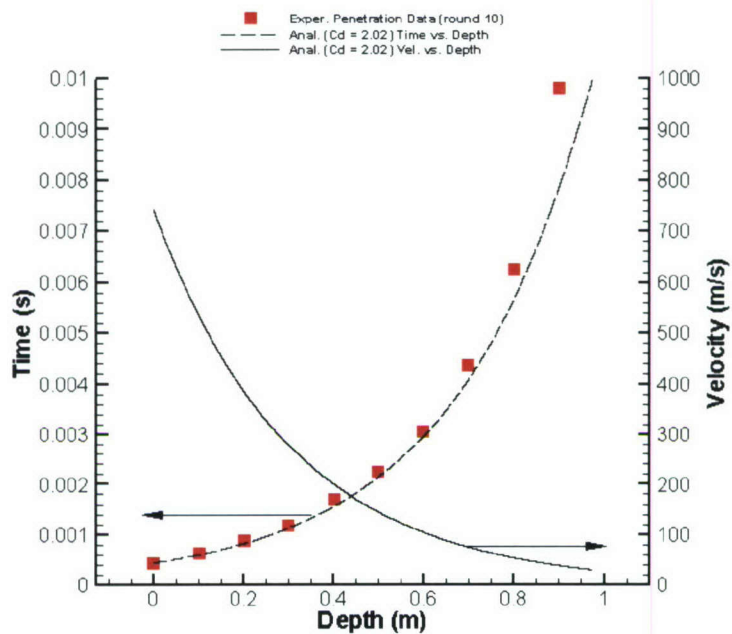


Figure 12: Velocity versus depth and time (experiment): Configuration II

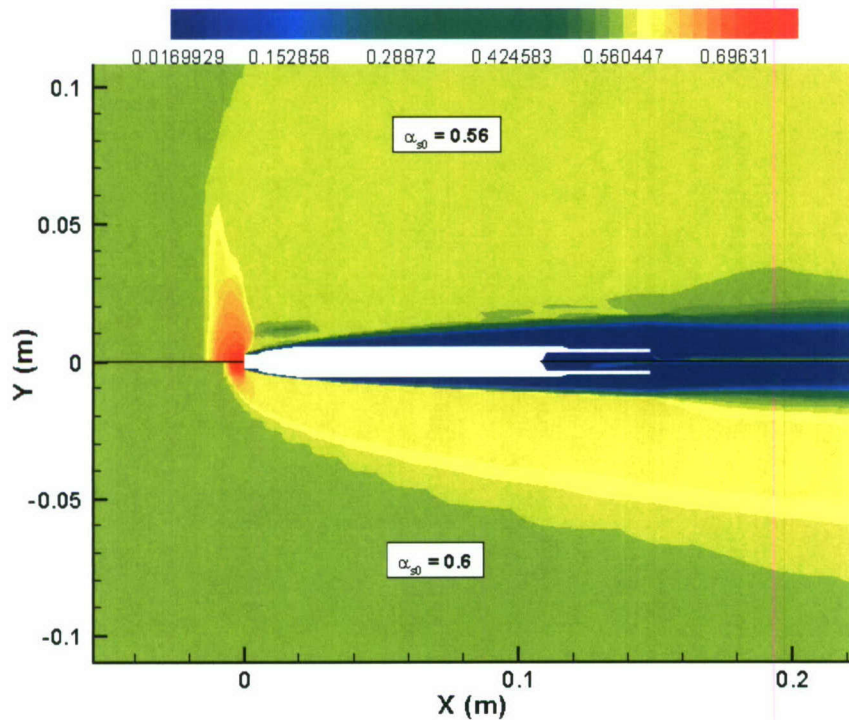


Figure 13: Solids voidage contours – effect of α_{s0} : Configuration III

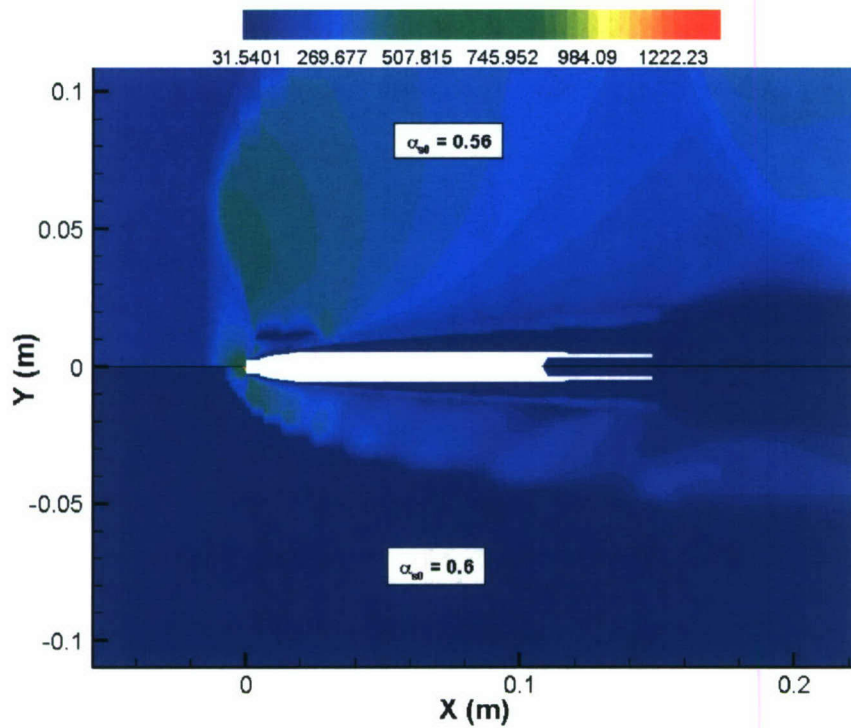


Figure 14: Solids sound speed contours: Configuration III

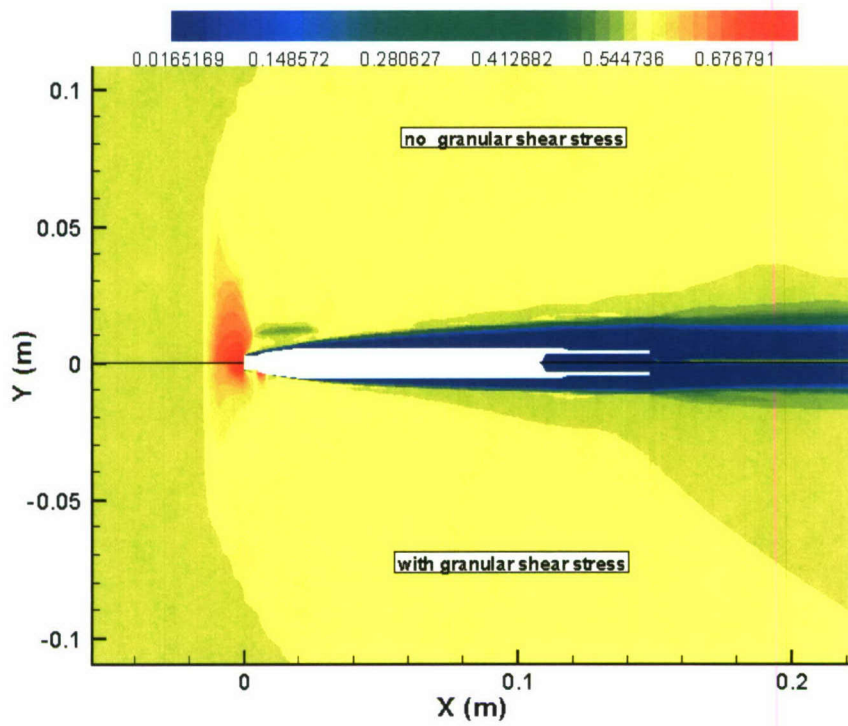


Figure 15: Solids voidage contours – effect of solids shear stresses: Configuration III

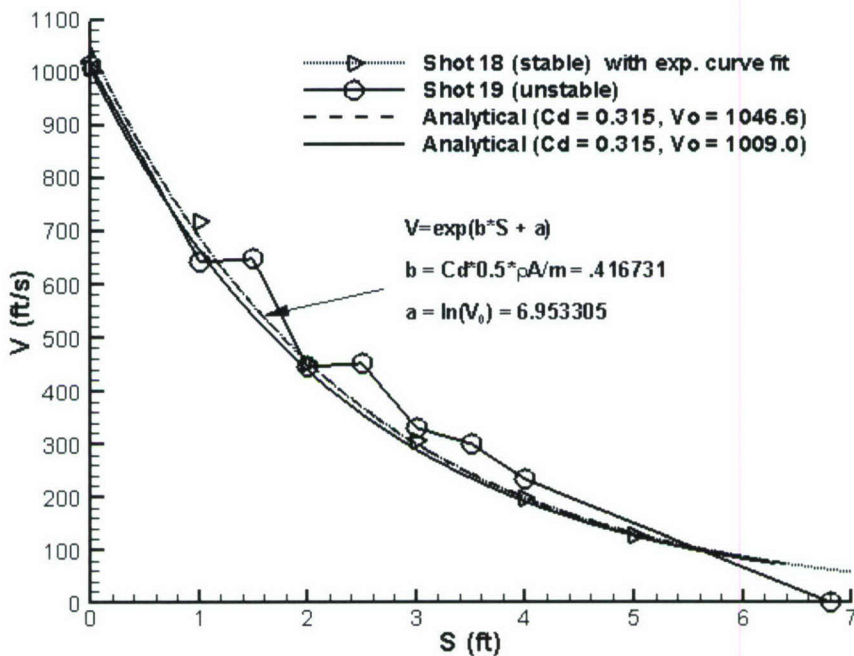


Figure 16: Velocity versus depth (experiment): Configuration III

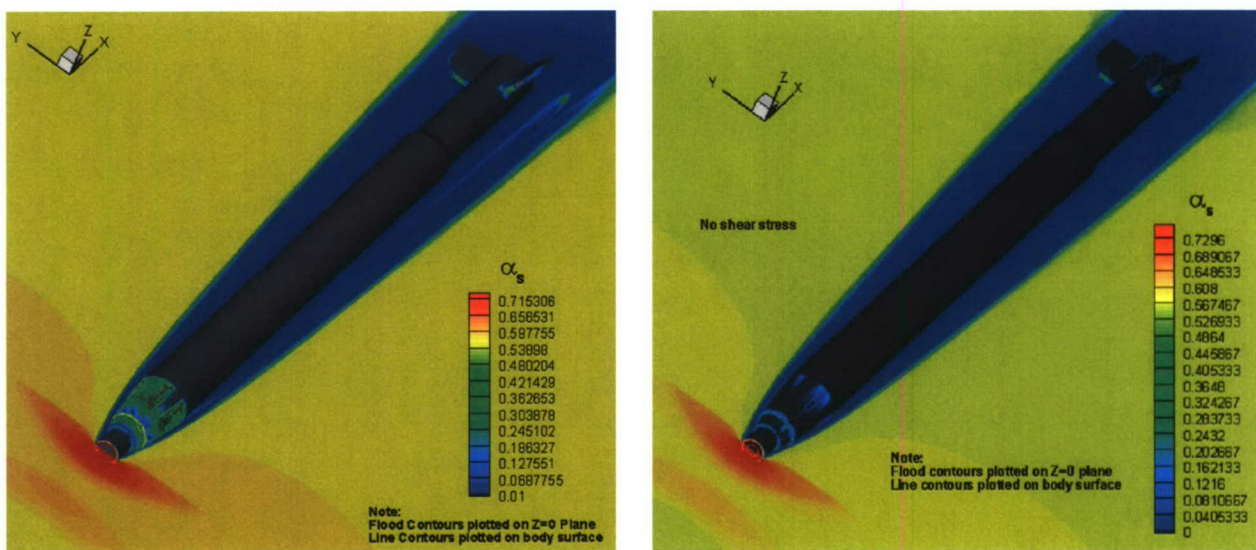


Figure 17: Solids volume fraction contours for 3-D simulation of dry sand flow over the Lockheed-Martin dart (including fins) Left – no solids shear stress; right – with solids shear stress

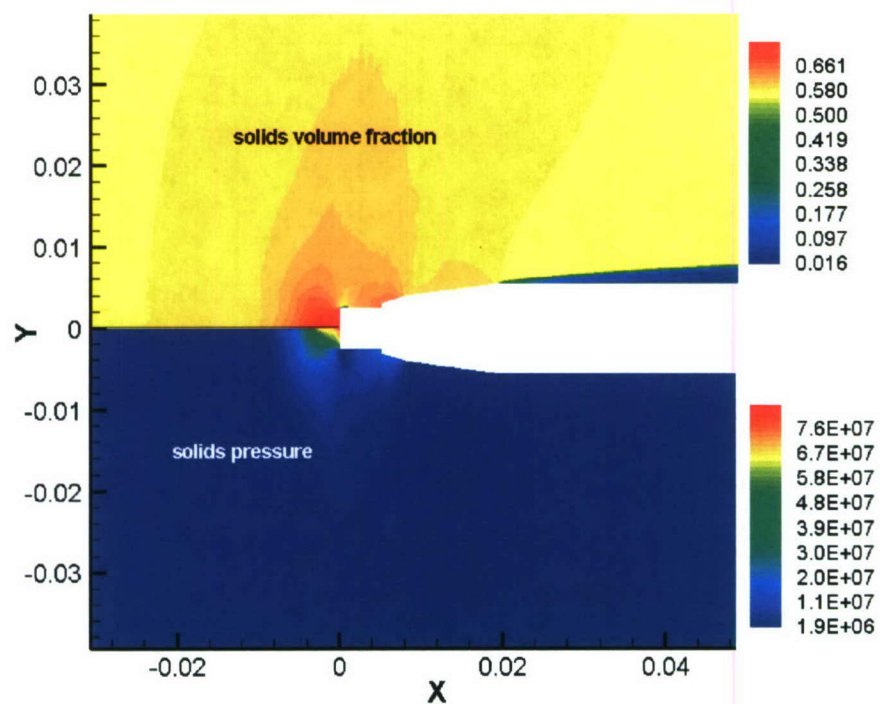
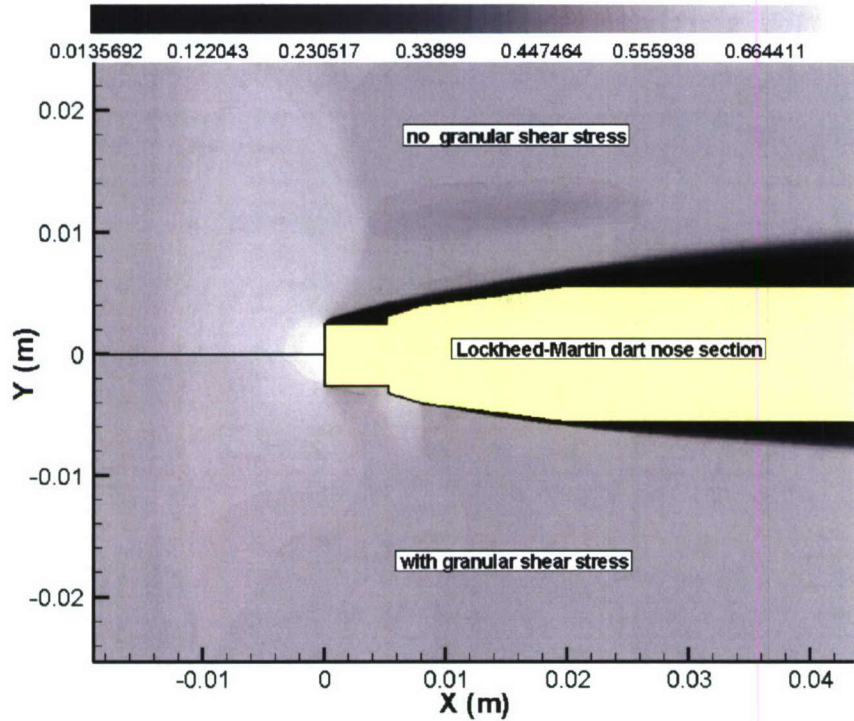


Figure 19: Solids volume fraction and solids pressure contours using improved solids-stress models.

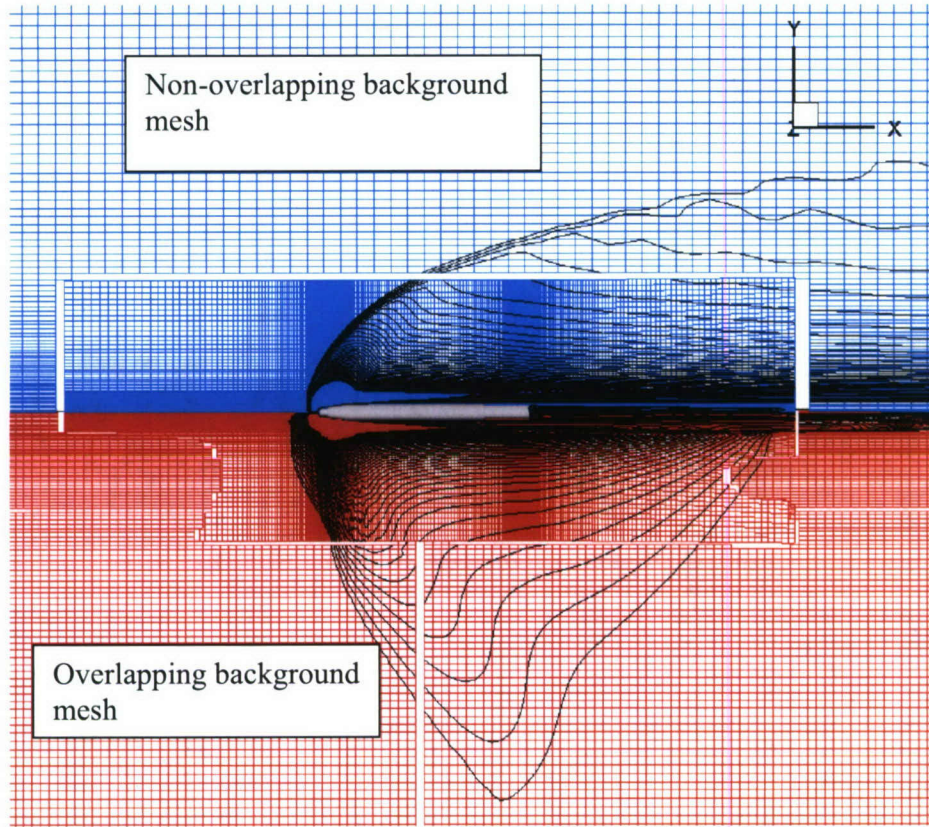


Figure 20: Solids vertical velocity predictions on two different composite meshes